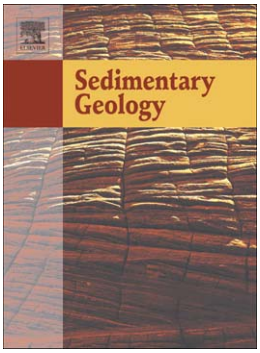

Cyclostratigraphy and chemostratigraphy of a bioclastic storm-dominated carbonate ramp (Late Pliensbachian, Iberian Basin)

Jorge Val, Beatriz Bádenas, Marcos Aurell, Idoia Rosales

PII: S0037-0738(17)30106-9
DOI: doi:10.1016/j.sedgeo.2017.04.007
Reference: SEDGEO 5189

To appear in: *Sedimentary Geology*

Received date: 31 January 2017
Accepted date: 25 April 2017

Please cite this article as: Val, Jorge, Bádenas, Beatriz, Aurell, Marcos, Rosales, Idoia, Cyclostratigraphy and chemostratigraphy of a bioclastic storm-dominated carbonate ramp (Late Pliensbachian, Iberian Basin), *Sedimentary Geology* (2017), doi:10.1016/j.sedgeo.2017.04.007

Cyclostratigraphy and chemostratigraphy of a bioclastic storm-dominated carbonate ramp (Late Pliensbachian, Iberian Basin)

Jorge Val[a*], Beatriz Bádenas[a], Marcos Aurell[a] & Idoia Rosales[b]

[a]Dpto. Ciencias de la Tierra, Universidad de Zaragoza, 50009 Zaragoza, Spain

[b]Instituto Geológico y Minero de España (IGME), E-28760 Tres Cantos, Madrid, Spain

* Corresponding author, e-mail address: jorgevalmunoz@gmail.com (Jorge Val)

ABSTRACT

Deposition of regressive successions and coeval positive trend in the oxygen stable isotope record in relatively deep marine successions of the upper Pliensbachian of western European basins have been related to a cooling interlude within the warm greenhouse conditions of the Pliensbachian. Sedimentological, cyclostratigraphic and chemostratigraphic analyses carried out in two upper Pliensbachian successions exposed in the Iberian Chain (Obón and San Pedro localities, Spain) allowed the characterization of the imprint of this cooling interlude on the relatively shallow areas of the Iberian carbonate ramp. The upper Pliensbachian succession is characterized by skeletal limestones and encompasses proximal mid-ramp to proximal outer-ramp facies, in which resedimentation and reworking by storm-induced flows controlled the accumulation of bioclastic debris. Two orders of high-frequency, metre-scale sequences have been identified: bundles of beds, and deepening-shallowing sets of bundles. According to the age calibration (previous biostratigraphic data and new strontium isotopes data) and correlation with nearby sections, these

sequences are suggested as formed in tune with the short-term and long-term eccentricity Milankovitch cycles. The isotopic data from brachiopod shells and belemnite rostra indicate progressively increasing $\delta^{18}O$ and slightly decreasing $\delta^{13}C$ trends for the uppermost Pliensbachian *Spinatum* Zone, reflecting the influence of cooling conditions. However, facies analysis reflects that the expected coeval long-term regression was interrupted by a tectonically driven transgressive event in the uppermost part of the *Spinatum* Zone.

Key-words: Pliensbachian, C and O isotopes, cyclostratigraphy, cooling interlude, Iberian Basin

1. Introduction

During the Early Jurassic, sedimentation in the Iberian Basin (NE Iberian Plate) took place in a ramp-type carbonate platform slightly deepening to the north. This intracratonic platform acted as a seaway, connecting the Tethys Ocean to the southeast with the Boreal epicontinental domain to the northwest. The marine facies recorded in the Iberian Basin during the late Pliensbachian corresponds to a transgressive-regressive facies cycle (Aurell *et al.*, 2003; Gómez & Goy, 2005). The regressive hemicycle is represented by a 10–20 m-thick succession of bioclastic limestones with some interbedded marls belonging to the Barahona Formation. The most abundant bioclastic grains found in this unit are bivalves, brachiopods and belemnites.

Deposition of limestone-dominated successions linked to a regressive stage at the end of the Pliensbachian has also been recognized in other western European basins. This regional regressive trend has been related to a cooling interlude that preceded the climate warming of the earliest Toarcian (Price, 1999; Dera *et al.*, 2011). Several authors have studied the isotopic record of the late Pliensbachian cooling episode in relatively deep-water successions in western European basins (e.g.,

Asturian Basin: Gómez & Goy, 2011; Gómez *et al*., 2015; Basque-Cantabrian Basin: Rosales *et al*., 2004; Causses Basin: Mailliot *et al.*, 2009; Lusitanian Basin: Suan *et al*., 2010; Subbetic Basin: Sandoval *et al*., 2012). Isotopic analyses carried out by those authors on belemnite rostra and bulk carbonate show higher $\delta^{18}O$ and lower $\delta^{13}C$ values for the latest Pliensbachian (in the Boreal *Spinatum* Zone, or in the equivalent Tethyan *Emaciatum* Zone) than those recorded for the early Toarcian. However, studies focusing on the sedimentary imprint of the latest Pliensbachian cooling interlude and earliest Toarcian warming on relatively shallow-water successions are very scarce. The facies, sequential and chemostratigraphic analyses of the Barahona Formation performed here offer new data on this subject, and allow us to discuss the similarities and differences between the sedimentary record of the latest Pliensbachian cooling episode in the Iberian Basin and coeval deeper-water successions studied in previous works.

This paper presents the results of a facies analysis and correlation of high-order sequences recorded in the upper Pliensbachian Barahona Formation carried out on two representative outcrops of the Aragonese Branch of the Iberian Range (NE Spain). Additional information is provided by a chemostratigraphic analysis of the C and O stable isotopes of the studied succession. Analysis of Sr isotopes combined to the previously published data on the ammonite biostratigraphy, allowed to reach a more precise age calibration of belemnite rostra and brachiopod shells. The main objectives of this work are: (1) to understand the palaeoenvironmental significance of facies and propose a sedimentological model for the upper Pliensbachian successions recorded in the central part of the Iberian Basin; (2) to establish the vertical facies trends characterizing the long-term regressive trend, as well as the superimposed high-frequency deepening and/or shallowing sequences; (3) to discuss the factors controlling sedimentation, including the influence of the cold to warm climate conditions and the possible imprint of higher-frequency climatic cycles; and (4) to compare the C and O isotopic signal obtained in the relatively shallow studied succession with those obtained in coeval deeper successions in nearby basins and to discuss the significance and extent of the controlling factors.

2. Geological setting and studied sections

Two stratigraphic sections of the upper Pliensbachian Barahona Formation have been studied and correlated. These sections are located in the Aragonese branch of the Iberian Chain (Teruel province, NE Spain), one near the locality of Obón (Obón section), and the other one between the localities of Oliete and Ariño (San Pedro section) (Fig. 1A). The sections are 15 km apart (distance without restoring the tectonic shortening).

The upper Pliensbachian succession in the study area represents deposition in relatively shallow domains of a large ramp-type carbonate platform that developed in large areas of the Iberian Basin (Goy *et al*., 1976; Comas-Rengifo *et al*., 1999; Bordonaba & Aurell, 2002). During the Early Jurassic, this carbonate ramp was open to the north and located at a palaeolatitude of ~30-35º N (Osete *et al*., 2011) (Fig. 1B). The platform underwent a progressive deepening from carbonate coastal environments for most of the Sinemurian to relatively deep platform facies, up to a maximum flooding in the middle Toarcian (Aurell *et al.*, 2003). Higher-order T-R facies cycles have been defined for the Pliensbachian-Toarcian of the Iberian Basin, including the upper Pliensbachian T-R facies cycle (Fig.1C). This cycle ranges from the upper part of the early Pliensbachian *Davoei* Zone to around the boundary of the Pliensbachian *Spinatum* Zone with the Toarcian *Tenuicostatum* Zone (Fig. 1C; Gómez & Goy, 2005). The open-marine marl-dominated Cerro del Pez Formation (lower *Margaritatus* Zone, *Stokesi* Subzone) corresponds to the transgressive hemicycle of the late Pliensbachian T-R facies cycle. The bioclastic limestones of the Barahona Formation (upper *Margaritatus* and *Spinatum* zones) record the regressive stage of this cycle (Fig. 1C). The upper boundary of the Barahona Formation roughly coincides with the Pliensbachian-Toarcian boundary and constitutes a regional transgressive surface indicated by the onset of the deposition of the ammonite-rich marl-limestone alternation of the Turmiel Formation.

In the studied area, the Barahona Formation is around 18 m thick and consists of three lithological intervals (Fig. 2A, B). The lower interval is formed by an alternation of dm-thick bedded mud-supported limestones and marls, in gradual transition to the underlying marly-dominated Cerro del Pez Formation. The middle part of the Barahona Formation corresponds to dm-thick tabular, mostly grain-supported bioclastic limestones. The upper interval is composed of nodular bioclastic limestones with intercalated marls and represents the transition to the overlying marl-limestone alternation of the Turmiel Formation.

Previous biostratigraphy data by Mouterde *et al*. (1978) on the basis of ammonite distribution are available for the Obón section, which will be discussed below in order to precise the location of the boundaries of the successive upper Pliensbachian ammonite biozones.

3. Methods

The upper Pliensbachian Barahona Formation in the Obón and San Pedro sections has been studied bed-by-bed in order to obtain detailed sedimentological and chemostratigraphic data. In the Obón succession, the studied interval has been extended up to the lowermost Toarcian (i.e. the lowermost part of the Turmiel Formation). The field data were completed with the petrographic analysis of rock samples in polished slabs and thin sections (32 samples).

3.1. Sedimentological analysis

The sedimentological analysis comprised the field description of depositional features, such as texture, components (type and abundance of carbonate grains), sedimentary structures (including trace fossils) and the bounding surfaces of beds.

Bioturbation intensity was assessed according to the Taylor & Goldring (1993) bioturbation index (BI), which categorizes it from 0 to 6, where 0 indicates no bioturbation. Moderate bioturbation was assigned to beds with 5 to 30% of bioturbation (BI 1 to 2) including *Diplocraterion*, *Planolites* and/or *Rhizocorallium* traces but still preserving sedimentary structures. Severe bioturbation was assigned to beds with 31 to 100% of bioturbation (BI 3 to 6) including *Chondrites* and *Thalassinoides* along with the above-mentioned traces that obliterate sedimentary structures.

The identification of sharp bedding surfaces bounding bundles of beds and recording omission and/or erosion surfaces was used as criteria for identifying high-order sedimentary sequences, as these sharp bedding surfaces are interpreted as reflecting sharp changes in sedimentation (e.g., Schwarzacher, 2000; Strasser *et al*., 1999; 2005; Bádenas *et al*., 2005). Vertical facies trends within the defined high-order sedimentary sequences were used to characterize them in terms of deepening- and/or shallowing-upward trends when possible.

3.2. Geochemical analyses

A total of 92 samples (51 belemnite rostra, 26 samples of brachiopod shells and 15 lime mudstone rock samples, see Table 1) were collected throughout the Obón section for the analysis of O and C stable isotopes (3 samples/m on average). These samples can potentially provide information on the O and C stable isotope values of habitats ranging from neritic-pelagic (near-surface) to benthic (bottom waters) (e.g. Wierzbowski, 2004; Wierzbowski & Joachimski, 2007; Colombié *et al.*, 2011; Armendáriz *et al*., 2012). In addition, 19 samples of belemnite rostra and brachiopod shells were selected along the entire Obón section for $^{87}Sr/^{86}Sr$ analysis, in order to discuss a more precise age calibration, and other 12 belemnite and brachiopod calcites were also analysed for major and trace element composition (Table 1). Comparison between the $^{87}Sr/^{86}Sr$ curve obtained and the global marine $^{87}Sr/^{86}Sr$ curve developed for the Early Jurassic (Burke *et al*.,

1982, Jones & Jenkyns, 2001, Global Time Scale (GTS): Gradstein *et al*., 2012) will provide an accurate age calibration of the studied upper Pliensbachian successions.

Belemnite rostra, brachiopod shells and lime mudstone internal sediment in brachiopod shells were examined under a binocular microscope. Before drilling to carry out the geochemical analysis, those areas of the belemnite rostra and brachiopod shells most susceptible to diagenetic alteration or that appeared altered under the binocular microscope (microfractures, chalky-cloudy areas and the exterior parts in contact with sediment) were removed with a dental drill. In addition, thin sections of belemnites were prepared to evaluate the possible diagenetic alteration under a petrographic microscope and under cathodoluminescence (CL) in order to select and sample the non-luminescent portions, which have traditionally been considered to be primary biogenic calcite that is mostly diagenetically unaltered (e.g. Sælen, 1989; Rosales *et al*., 2001). The CL analysis was carried out with a Technosyn Cold Cathodo Luminoscope at IGME (Spain), under 10–12 kV beam potential, a 0.5 μA beam current and 0.05–0.1 torr pressure. Belemnite and brachiopod calcites that appeared non-luminescent in CL and that were seen as translucent under a binocular microscope were powdered with a dental drill.

The elemental concentrations (Ca, Fe, Mg, Mn, Na, Sr) of belemnite and brachiopod calcites were analysed at the IGME laboratories using a Varian Vista MPX ICP-AES spectrometer after dissolving the carbonate powders in 10% hydrochloric acid. The detection limits for Ca, Fe, Mg, Mn, Na and Sr are 1000, 250, 100, 20, 100 and 10 μg/g respectively.

Samples for O and C isotope analyses were processed on a SIRA-II mass spectrometer at the Servicio de Análisis de Isótopos Estables of the Universidad de Salamanca (Spain). Carbon- and oxygen-isotope ratios are expressed in the usual δ-notation in parts per mile (‰) relative to the Vienna Pee Dee Belemnite (V-PDB) standard. Samples were calibrated against the internal carbonate standard EEZ-1, which had previously been compared with the international standard

NBS-19 (values of 1.95‰ and –2.20‰ for $\delta^{13}C$ and $\delta^{18}O$, respectively). The $^{87}Sr/^{86}Sr$ isotopes were determined with a TIMS-Phoenix thermal ionization mass spectrometer at the CAI de Geocronología y Geoquímica Isotópica of the Universidad Complutense de Madrid (Spain). All $^{87}Sr/^{86}Sr$ data were corrected for possible ^{87}Rb interferences and were normalised to a value of 0.1194 for $^{86}Sr/^{88}Sr$. During the period of analysis, the NBS-987 standard gave an average $^{87}Sr/^{86}Sr$ value of 0.710248 ± 0.00012 (2σ, n=8). This value was used to correct the measured values from a possible deviation referred to the standard. The analytical error of the $^{87}Sr/^{86}Sr$ ratio referred to 2σ was 0.01%.

4. Facies analysis and sedimentary interpretation

4.1. Facies description

Figures 3 and 4 include the sedimentary logs of the upper Pliensbachian Barahona Formation in the Obón and San Pedro sections. The unit is dominated by skeletal limestones and intercalates marls and marly limestones in its lowermost and uppermost parts. The main components are skeletal grains that include two different size-fractions: a fine fraction formed by more or less rounded, mm-sized bioclasts (mainly bivalves, brachiopods and echinoderms), and a coarser heterogeneous fraction composed of entire or disarticulated bivalves (*Gryphaea* and *Pholadomya*), brachiopods (e.g. *Aulacothyris*, *Lobothyris*, *Rhynchonella*, *Terebratula* and *Zeilleria*) and belemnites. On the basis of the character of the skeletal components and the texture and lithology, seven facies have been differentiated: marly facies (*m*), marly-limestone facies (*mL*), and limestone facies, including mudstone (*M*), wackestone (*W)*, fine packstone (*fP*), coarse packstone (*cP*), and lumachelle (*L*) (Fig. 5).

The limestone facies (*M, W, fP, cP* and *L*) are arranged in tabular or nodular dm-thick beds. The grain-supported facies *cP* and *fP* are formed by a fine bioclastic fraction and scattered complete

or disarticulated fossils, and are differentiated on the basis of the character of the fine bioclastic fraction. In *fP* this fine fraction is formed by well-sorted, rounded skeletal grains, < 2 mm in mean diameter, whereas in *cP* it corresponds to poorly-sorted, less rounded bioclasts, > 2 mm in mean diameter (Fig. 5C, D). Facies *L* is represented by dm-thick lumachelle beds (2 lumachelle beds in Obón and 3 lumachelle beds in San Pedro: see Figs. 3 and 4), which are almost entirely composed of complete fossils of bivalves and brachiopods surrounded by a fine bioclastic matrix (Fig. 5E). The matrix-supported facies *M* and *W* are dominated by micrite, with variable percentages of fine bioclastic fraction (poorly-rounded bioclasts < 2 mm in mean diameter). Disarticulated or entire bivalves and brachiopods are frequent in *W*, but scarcer in *M* (Fig. 5A, B). These limestone facies show variable bioturbation, which usually concentrates at the top of the beds. Facies *M* has a low variety of trace fossils (mainly *Planolites* traces), whereas facies *W*, *fP* and *cP* show more abundant and varied bioturbation (*Chondrites*, *Diplocraterion*, *Planolites*, *Rhizocorallium* and *Thalassinoides* traces). Facies *L* has no trace fossils.

Facies corresponding to mixed lithologies (marls: *m* and marly limestones: *mL*) form thin cm-thick (and occasionally dm-thick) beds in the lower and upper part of the Barahona Formation. Both facies include a similar proportion of entire or disarticulated skeletal remains than facies *M* but show very scarce bioturbation. Locally, dm-thick marl beds show a higher fossiliferous content, mainly entire brachiopods and belemnites.

The dominant limestone facies *M*, *W*, *fP* and *cP* are vertically associated within individual beds, i.e. forming vertical arrangements of grain-supported bioclastic (*fP* and/or *cP*) levels and mud-supported (*M* and/or *W*) levels (Fig. 6). In particular, the following vertical arrangements of facies have been observed: a) thin levels (< 1cm in thickness) of facies *cP* intercalated in facies *fP*, *W* or *M*, with a sharp flat base and top, a crude fining-upward trend and occasional complete or disarticulated fossils disposed in a position of lower resistance to the flow (Fig. 6A); b) *cP*-*fP* or *cP*-*fP*-*W*-*M* vertical arrangements, with a sharp, usually irregular erosive base and a clear fining-upward trend (Fig. 6B); and c) several grain-supported cm-thick bioclastic levels with slightly

irregular erosive bases and a crude fining-upward trend (*cP* or *fP* amalgamated levels), in which reworking by bioturbation obliterates the internal structure (Fig. 6C).

4.2. Interpretation

The limestone-dominated successions of the upper Pliensbachian Barahona Formation represent deposition in relatively shallow areas of a ramp-type carbonate platform open towards the north (Bordonaba & Aurell, 2002; Aurell *et al.*, 2003). The character of facies described here allows a more accurate sedimentary model to be obtained for these successions, ranging from proximal middle-ramp domains to proximal outer-ramp domains (Val *et al*., 2014), characterized by storm-induced bioclastic accumulations (facies *cP* and *fP*) grading distally to progressively muddier sediments (facies *M, W, mL* and *m*) (Fig. 7). Deposition in these middle to outer ramp areas was characterized by the accumulation of skeletal grains, mainly from echinoderms, bivalves, brachiopods and belemnites, and by the absence of other types of carbonate grains.

The presence of two skeletal fractions (i.e. a fine bioclastic fraction and complete or disarticulated fossils) indicates the different origin and reworking processes of these skeletal components. The small size and roundness of the fine bioclastic fraction suggest that these grains would be maintly allochthonous skeletal grains that were probably broken and rounded in relatively shallow, wave-agitated areas (i.e. inner ramp, above a fair-weather wave base). By contrast, the entire and disarticulated fossils of bivalves, brachiopods and belemnites would correspond to para-autochthonous skeletal grains (benthic and nekto-planktonic organisms).

The sedimentological features in facies *fP* and *cP* (grain-supported texture, dominance of allochthonous fine bioclastic fraction) indicate deposition in high-energy ramp domains. However, the presence of muddy matrix and para-autochthonous fossils, as well as the abundance of trace fossils, reflects intermittent wave agitation. Therefore, these facies were not formed in inner ramp areas subjected to constant fair-weather wave action, but most probably in the proximal area of the

middle ramp, below the fair-weather wave base but subjected to storm-induced waves and currents (Fig. 7). The allochthonous bioclastic grains and lime mud in these facies would be resedimented from the shallower inner-ramp areas towards distal domains by storm-induced offshore-directed return flows. The coarser and less rounded allochthonous bioclastic grains in facies *cP* compared to facies *fP* indicate a lower distance of transport and a nearer location to the source area for the allochthonous grains, so that deposition of *cP* probably took place in more proximal areas of the middle ramp compared to *fP*. The presence of frequent amalgamated bioclastic *cP* and *fP* levels (see Fig. 6C) indicates deposition from successive storm-induced flows carrying reworked skeletal grains away from inner ramp areas (i.e. amalgamated tempestites typical of the proximal mid-ramp areas: Burchette & Wright, 1992).

The matrix-supported facies *M* and *W* represent lower-energy domains with an occasional record of higher-energy distal flows represented by thin grain-supported *cP* levels with a crude fining-upward trend (see Fig. 6A). Their deposition probably took place in the distal middle-ramp domain, where the storm-induced return flows progressively lose energy, the proportion of resedimented allochthonous skeletal grains is reduced, and the bioclastic fraction is diluted in the lime muds carried by the flows (i.e. diluted tempestites). Facies *W*, with a higher proportion of allochthonous skeletal grains, would be deposited in a slightly more proximal location than facies *M*. The presence of *cP-fP-W-M* levels and *cP-fP* levels with an erosive base and a fining-upward trend (see Fig. 6B) and thin levels of *cP* within *fP* beds (Fig. 6A) would correspond respectively to the deposition of complete tempestites (*cP-fP-W-M*) and incomplete tempestites (*cP-fP*).

The discrete beds with accumulations of entire para-autochthonous fossils (mainly brachiopods and bivalves) in lumachelle facies *L* do not show any evidence of storm-induced hydrodynamic accumulations. The scarce bioturbation and absence of fossil traces in those dm-thick levels, and their preservation in the context of a relatively high-energy domain rule out their possible interpretation as a biostrome built through the accumulation of several generations. More likely, facies *L* can be interpreted as the record of mass-mortality events (e.g., Kidwell, 1991). The

presence of similar number of lumachelle beds correlatable in the 15 km apart studied sections, which are intercalated in the proximal middle-ramp facies *cP* and *fP* would reflect that the mass-mortality events were possibly recorded in a relatively large area of the platform.

The deposition of the mixed facies *m* and *mL* is related to proximal areas of the outer ramp, where resedimentation of the fine allochthonous bioclastic fraction from shallow areas was lower and sedimentation was dominated by the settling of resedimented carbonate particles and terrigenous mud and silt fraction (Fig. 7). The terrigenous muds included in these mixed facies would be originated by river flood events or surface flood plumes, and transported from the continent in near-bottom hyperpycnal that could be dispersed seaward by storms (e.g. Fan et al., 2004). In some cases, facies *m* appears as thin intercalations within limestone beds, bounding bundles of limestones beds (see Figs. 3 and 4). These fine levels probably represent episodes of higher fine terrigenous supply and/or lower carbonate resedimentation. In the studied area, there is no record of the counterpart deeper, lower-energy (distal outer-ramp) facies and to the shallower, higher-energy (inner-ramp) facies.

5. High-order sequences and facies correlation

The analysis of high-frequency sequences in the Barahona Formation has been performed as a tool for the interpretation of the internal and external factors controlling changes in relative sea-level and sedimentation patterns in the basin. The correlation of equivalent high-frequency sequences in the two studied sections also provides additional data to corroborate the sedimentological interpretation of facies, i.e. the gradual transition of facies in a ramp-type platform, from high-energy, proximal mid-ramp areas to low-energy, proximal outer-ramp areas (i.e., the *cP-fP-W-M-mL-m* lateral facies transition in Fig. 7). Two orders of high-frequency sequences: higher-order

sequences (bundles of beds) and lower-order sequences (sets of bundles) have been recognized and correlated between the two studied sections (Fig. 8).

5.1. Bundles of beds

The higher-order sequences recognized correspond to bundles of beds (B) bounded by prominent sharp bedding surfaces (see Fig. 2), which represent erosion or non-sedimentation surfaces (Schwarzacher, 2000). Sixteen dm-to m- scale bundles of beds have been identified in both stratigraphic sections (see B1 to B16, Figs. 3 and 4). The similar number of bundles and the existence of correlatable lumachelle key beds (facies *L*) support the one-to-one correlation of the bundles defined in the two sections. In addition, the similar vertical sedimentary trends and thickness of most of the equivalent bundles support this is the best-fitting correlation (Fig. 8).

Sequences B1 and B2 are dominated by muddy facies. B1 has a clear deepening-shallowing facies trend in San Pedro (with outer ramp facies *m* located in its middle part), but a deepening trend in Obón, as the shallowing part is affected by erosion at the base of B2. The step up in the $^{87}Sr/^{86}Sr$ values obtained just below and above this surface in the Obón section (Fig. 3) may provide further evidence for the presence of this erosive gap (McArthur *et al*., 2016). B2 is a deepening-upward sequence in both sections, as indicated by the vertical facies trend from *P* to *mL-m* facies.

Sequence B3 is dominated by facies *fP* with alternations of muddy facies *W* and *M* and mixed facies *mL*, but without any clear vertical facies trend (i.e. aggradational facies trend). Sequence B4 is characterized by a shallowing facies trend in both sections and includes shallower facies *cP* in Obón and relatively deeper facies (*m*, *W* to *fP*) in San Pedro. This facies distribution agrees with the lateral relationship of the facies in the carbonate ramp under study (see Fig. 7) and indicates that at this time, the Obón section would be located in a shallower position compared to San Pedro.

Sequences B5 to B10 are dominated by grain-supported facies *fP*. The presence of a lumachelle key bed (facies *L*) in B8 and B10 provides an additional guideline for correlation. These

sequences reflect a homogeneous lateral distribution of grain-supported facies (aggradational facies trend) except in B5, which shows a lateral relationship of shallow facies *fP* in Obón to deeper *M* facies in San Pedro.

Sequences B11 and B12 are dominated by grain-supported facies *cP*. B11 shows the progradation of shallower facies *cP* dominant in Obón over the deeper facies *fP* in San Pedro, supporting the deeper domains located in the San Pedro area. Sequence B12 shows a significantly reduced thickness in Obón compared to San Pedro (1 and 2 m, respectively) and a prominent sharp erosive surface on top in the two logged sections (i.e., the boundary between the lower and upper Barahona Formation, see Fig. 2A, B) indicating the presence of a significant sedimentary discontinuity (see D1 in Fig. 8).

Sequences B13 to B16 record a transgressive event in both sections (a marly bed overlies the *cP* facies and D1 surface on top of B12: Fig. 8), as well as a significant change in facies polarity, as deeper muddy facies predominate in Obón. The facies distribution obtained by correlation of bundles confirms this facies polarity. Sequence B13 has a vertical deepening facies trend in Obón (*fP* to *W*) but an aggradational *fP* facies trend in San Pedro. Sequences B14 and B15 have shallowing facies trends in Obón, whereas in San Pedro those sequences are composed by sets of amalgamated facies *fP* beds, culminating B15 with a shallow facies *cP* bed. Sequence B16 shows a clear shallowing facies trend in Obón, but is partially covered in San Pedro. An erosive surface (see D2 in Fig. 8) is located on top of B16 in Obón (see Fig. 2A), which correlates with the basin-wide discontinuity surface found around the Pliensbachian-Toarcian boundary (e.g., Gómez & Goy, 2005). As is explained below, the presence of a significant sedimentary hiatus at the earliest Toarcian in the Obón section is supported by biostratigraphic and chemostratigraphic data.

5.2. Sets of bundles

The analysis of long-term vertical facies trends has allowed four deepening-shallowing lower-order sequences to be identified. These sequences correspond to sets of bundles B1–B4, B5–B8, B9–B12, and B13–B16 respectively, which are around 3 to 5 m in thickness (Fig. 8).

Set B1–B4 includes a deepening part recorded by bundles B1 and B2, which are dominated by muddy facies. The facies *mL* bed that culminates B2 is interpreted as the maximum flooding interval. The shallowing part of the set corresponds to B3 and B4 and reflects the clear progradation of shallower grain-supported facies.

Set B5–B8 is dominated by facies *fP* and, on the basis of the vertical facies trend could be interpreted as a deepening-shallowing sequence with the maximum flooding interval located in B6; its shallowing part culminates with facies *cP* and a correlatable continuous facies *L* key bed in B8.

Set B9–B12 is dominated by grain-supported facies and has also a deepening-shallowing evolution, with the maximum deepening interval indicated by the marly limestone bed at the top of B10. The deepening part has facies *fP*, and the shallowing part reflects the sharp progradation of facies *cP* through the studied sections.

Set B13–B16 reflects a major deepening episode with an important change in facies polarity; it also records a deepening-shallowing facies trend with its maximum flooding interval in the muddy *M* facies at B15.

At a larger scale, sets B1–B4 to B9–B12 represent a longer-term shallowing facies trend. During this time interval, shallower facies dominate in Obón compared to San Pedro, which is located in a more northerly area (see Fig. 1). This distribution fits the overall palaeogeographical polarity of the Pliensbachian ramp, deepening to the northwest (Bordonaba & Aurell, 2002). However, set B13–B16, located in the uppermost part of the Barahona Formation, records a sharp deepening event and a change in facies polarity over a discontinuity surface (D1), followed by another widespread discontinuity surface (D2) at the top of the Barahona Formation.

6. Age calibration of the Obón section

The age calibration of the Barahona Formation in the Obón section supported by ammonite and $^{87}Sr/^{86}Sr$ isotope data has provided a trustworthy chronostratigraphic frame to calibrate the high-order sedimentary sequences and the stable O and C isotope data in the upper Pliensbachian deposits of the northeastern Iberian Basin (Fig. 9A).

In the Obón section, Mouterde *et al.* (1978) located the boundary between the *Margaritatus* and *Spinatum* zones towards the lower part of the Barahona Formation, on the basis of the last appearance of *Protogrammoceras* sp. and the first appearance of *Pleuroceras spinatum*. Therefore, there was an uncertainty interval for the location of the *Margaritatus-Spinatum* zone boundary, ranging from the top of our bed 2 up to the top of bed 34 (Fig. 9A). The boundary between the *Spinatum* and *Tenuicostatum* zones (i.e. Pliensbachian-Toarcian boundary) was located by Mouterde *et al.* (1978) in the uppermost part of the Barahona Formation on the basis of the last appearance of *Pleuroceras spinatum* on bed 46 and the first appearance of *Dactylioceras semicelatum* on bed 57.Therefore, there was an uncertainty interval for the location of the *Spinatum-Tenuicostatum* zone boundary from the top of bed 46 up to the top of bed 56 (i.e. the top of the Barahona Formation: Fig. 9A). It is important to remark that *Dactylioceras semicelatum* belongs to the upper *Tenuicostatum* Zone (i.e. *Semicelatum* Subzone), so the biostratigraphic data reported by Mouterde *et al*. (1978) indicate the absence of the lowermost *Tenuicostatum* Zone record (i.e. *Mirabile* Subzone) in the Obón area.

The obtained $^{87}Sr/^{86}Sr$ curve (Fig. 9A) shows a decreasing trend from the lowermost part of the Barahona Formation in the *Margaritatus* Zone ($^{87}Sr/^{86}Sr$ on average = 0.70720) up to the top of the Barahona Formation (top of bed 56, $^{87}Sr/^{86}Sr$ = 0.70707). At the lowermost part of the Turmiel Formation the $^{87}Sr/^{86}Sr$ curve shows a sharp change to an increasing trend (up to $^{87}Sr/^{86}Sr$ = 0.70720 in bed 65). The comparison of this $^{87}Sr/^{86}Sr$ curve and the Lower Jurassic global $^{87}Sr/^{86}Sr$ curve (Fig.

9B; Gradstein *et al*., 2012; Ullmann *et al.*, 2013; Metodiev *et al*., 2014) has enabled to reduce the uncertainty interval for the *Margaritatus-Spinatum* and the *Spinatum-Tenuicostatum* zones boundaries:

1) The *Margaritatus-Spinatum* boundary uncertainty interval has been located between the top of bed 16 ($^{87}Sr/^{86}Sr$ = 0.70717) and the top of bed 34 ($^{87}Sr/^{86}Sr$ = 0.70714) according to the $^{87}Sr/^{86}Sr$ values, which fit with the global $^{87}Sr/^{86}Sr$ curve (Fig. 9B: Gradstein *et al*., 2012: $^{87}Sr/^{86}Sr$ = 0.70712) and the available ammonite data (Mouterde *et al.*, 1978). Those values are within the range defined by Ruhl *et al*. (2016) in UK and Portugal (Fig. 9B: $^{87}Sr/^{86}Sr$ = 0.70712 to 0.70718).

2) The *Spinatum-Tenuicostatum* zones boundary (Pliensbachian-Toarcian boundary) has been located at the top of bed 56 (i.e. the lithological boundary between the Barahona and Turmiel formations: D2 surface) according to the $^{87}Sr/^{86}Sr$ value ($^{87}Sr/^{86}Sr$ = 0.70707 in bed 56), which coincides with the value proposed by the GTS (Gradstein *et al*., 2012). The value in marly bed 57 located at the top of the discontinuity surface D1 (Fig. 9A) is very similar ($^{87}Sr/^{86}Sr$ = 0.707066), but the biostratigraphic data indicate that this bed corresponds to the *Semicelatum* Subzone (of the upper *Tenuicostatum* Zone). At any rate, $^{87}Sr/^{86}Sr$ value in bed 57 fits with the values proposed by Gradstein *et al*. (2012) for the upper *Tenuicostatum* Zone.

3) The$^{87}Sr/^{86}Sr$ values for the lowermost part of the Turmiel Formation above bed 57 are higher than the distinctive values for the *Tenuicostatum* Zone (Fig. 9B: Gradstein *et al*., 2012), marking a sharp change in the curve. Those $^{87}Sr/^{86}Sr$ values fit better with those recorded for the upper *Serpentinum* Zone (~0.70720 standard values according to Gradstein *et al*., 2012), therefore indicating the possible existence of a hiatus or sedimentary condensation affecting the lower *Serpentinum* Zone. This stratigraphic gap indicates the existence of a significant earliest Toarcian discontinuity, located on top of bed 57 (referred as discontinuity D3).

The age calibration proposed for Obón is also compared with the precise age calibration obtained by Comas-Rengifo *et al*. (2010) after extensive ammonite biostratigraphy and $^{87}Sr/^{86}Sr$ isotope data from the nearby Almonacid de la Cuba section (Fig. 9B). This section is located 45 km

north to Obón and corresponds to a relatively deeper area of the Iberian Basin. The $^{87}Sr/^{86}Sr$ curve in Almonacid de la Cuba obtained for the *Spinatum* and *Tenuicostatum* zones fits well the Obón data and supports the proposed ammonite biozones distribution. It is important to remark that whereas lowermost *Tenuicostatum* Zone is absent in Obón, in Almonacid de la Cuba is well recorded with the appearance of *Dactylioceras mirabile* before the subsequent appearance of *Dactylioceras semicelatum.* These data indicate that the absence of a lowermost *Tenuicostatum* Zone record in Obón should be assigned to local factors.

7. Analysis of carbon and oxygen stable isotopes

7.1. Degree of sample preservation

For the isotopic analyses, the degree of sample preservation was assessed by petrographic and cathodoluminescence (CL) observations (Fig. 10), along with analysis of elemental concentrations of selected samples. Cathodoluminescence microscope analysis of belemnite rostra revealed good textural preservation in the majority of the samples, which were mainly non-luminescent (Fig. 10 D-D'), with luminescence limited only to certain easily avoidable areas. Luminescence is restricted to the apical canal (Fig. 10 C-C'), some radial fibres (Fig. 10 E–E'), and areas adjacent to microstylolites (Fig. 10 C-C'). Some specimens show marked concentric rings of cloudy appearance, although most of the studied material lacks these concentric features under both petrographic and CL microscopy. In contrast, under CL the bulk carbonate sediment is orange luminescent (Fig. 10 D-D'). Examination of brachiopod shells (terebratulides) under a binocular microscope revealed good textural preservation of translucent calcite.

Investigation of separate carbonate fractions (belemnites, brachiopods and their internal muddy sediment) aimed to compare further isotopic analyses derived from coeval carbonate archives that potentially represent different water masses. By comparison with modern

representatives, the brachiopod shells are considered to be secreted in equilibrium or near-equilibrium with ambient seawater (e.g. Carpenter & Lohmann, 1995; Brand *et al*., 2003), therefore recording the isotopic signal of the sea bottom. On the other hand, belemnites are considered to have been nektonic to nektobenthonic and neritic-pelagic free swimmers, probably migrating, like modern *Sepia*, from shallow and warmer waters to deeper and cooler waters during seasons or ontogeny (Rexfort & Mutterlose, 2009). This implies that belemnites could have secreted their rostra in a wide range of palaeoenvironments, recording a mixed signal from bottom to near-surface waters. This style of life has been proposed due to the scatter in the isotopic signals usually shown by belemnites (e.g. McArthur *et al*., 2007). Nevertheless, the fact that belemnites are common in black-shale (anoxic) deposits lacking any benthic or nektobenthonic mode of life argues for a more nektonic style of life in near-surface, open seawater (Rexfort & Mutterlose, 2009). In addition, recent studies on the ultrastructure of belemnites have demonstrated that belemnite rostra were originally highly porous and that this porosity was rapidly filled with syntaxial overgrowths of abiotic calcite (Hoffmann *et al*., 2016; Benito *et al*., 2016). It remains uncertain whether these calcite overgrowths precipitated while the organisms were still alive or during early marine diagenesis. These findings have increased the uncertainty about the meaning of the isotopic signal recorded by belemnites for palaeoceanographic studies. Finally, the carbonate sediment analysed in brachiopods (micritic) is assumed to be made of a mixture of lime mud and silt-sized skeletal components transported from shallow environments to the middle-proximal outer carbonate ramp, according with the sedimentary processes deduced from facies analysis. It would therefore represent a carbonate archive of the inner water mass of the ramp. The orange luminescence of the carbonate matrix suggests diagenesis during carbonate mineralogical stabilization. As long as no evidence of the influence of phreatic meteoric waters has been detected in these middle- to outer-ramp environments, this diagenetic stabilization is assumed to have occurred during early diagenesis in a closed system of marine pore waters.

The trace element analysis of selected samples (belemnite and brachiopod calcites, Table 1) shows Fe and Mn concentrations for all the analysed belemnite rostra below the detections limits (250 μg/g and 20 μg/g respectively), and Sr values above 923μg/g. These values are well below the cut-off values for Fe and Mn, and above the cut-off values for Sr, established as criteria for discriminating diagenetically altered and non-altered belemnite samples (e.g. Rosales *et al*., 2001; Alberti *et al*., 2012). In contrast, the trace element composition of the brachiopod calcites shows higher Fe and Mn concentrations and lower Sr concentrations than those observed for belemnites (Table 1). However, the obtained values are in general within the range of values reported for other brachiopod shells both modern (Morrison and Brand, 1986) and Pliensbachian (Rosales *et al*., 2001), supporting also a good stage of preservation. The only exception is the sample OB-48-BR (Table 1), which shows very high Fe (> 2000μg/g) and Mn (>40μg/g) concentrations, very low Sr (273 μg/g) concentration, and anomalous more radiogenic $^{87}Sr/^{86}Sr$ values, suggesting diagenetic alteration. This sample was excluded for further isotopic interpretation.

7.2. Carbon and oxygen isotope trends

The C and O stable isotope records obtained from the Obón section are represented in Figure 3 and Figure 9A. Two curves have been plotted for both the C and O isotope analysis, separated into two groups of data, i.e. those taken from belemnites, and those obtained from brachiopods and carbonate matrix sediment, given the similar values presented by brachiopods and carbonate internal sediment for coeval samples.

The $\delta^{18}O$ isotope curves from belemnites and brachiopods show different value ranges. The belemnite data show higher values of $\delta^{18}O$ (from -0.85‰ to 0.85‰) than those obtained from brachiopods (-3.69‰ to -1.16‰). The abundance of belemnite samples allows us to characterize a better-defined $\delta^{18}O$ trend compared to that of brachiopods, whose $\delta^{18}O$ values are almost

homogeneous and without a clear trend. According to the proposed age calibration, the $\delta^{18}O$ data from belemnites indicate a progressively increasing trend from the *Margaritatus* Zone (average $\delta^{18}O$ value ≈ -0.23‰) to the *Spinatum* Zone (average $\delta^{18}O$ value ≈ 0.25‰), which culminates at the top of the *Spinatum* Zone with the highest recorded values (average values of 0.43‰ for belemnites). For the lower Toarcian (upper *Tenuicostatum-Serpertinum* zones) a decreasing trend is recorded (average $\delta^{18}O$ value ≈ -0.5‰).

The $\delta^{13}C$ isotope values obtained from belemnites and brachiopods are very similar. The $\delta^{13}C$ values range from -0.25‰ to 2.17‰ (belemnites) and -0.38‰ to 2.40‰ (brachiopods). The $\delta^{13}C$ curves obtained through the *Margaritatus* Zone show very persistent values without any remarkable variations (average $\delta^{13}C$ value in belemnites ≈ 1.55‰; and in brachiopods ≈ 1.45‰) and a homogeneous vertical trend. Through the *Spinatum* Zone, the $\delta^{13}C$ curves show lower average and more scattered values (average $\delta^{13}C$ value in belemnites ≈ 1.17‰, and in brachiopods ≈ 0.89‰) and record a slightly decreasing trend from the base of the *Spinatum* Zone (average $\delta^{13}C$ value in belemnites ≈ 1.44‰, and in brachiopods ≈ 1.1‰), to the uppermost part of the *Spinatum* Zone (average $\delta^{13}C$ value in belemnites ≈ 0.5‰, and in brachiopods ≈ 0.25‰).The isotope data from belemnites in bed 57, overlying the *Spinatum-Tenuicostatum* zones boundary (D1 surface), show a significant leap in $\delta^{13}C$ values ($\delta^{13}C$ value = 1.77‰), which is not recorded in brachiopods and carbonate matrix (see Fig. 3). The lower Toarcian succession records higher $\delta^{13}C$ values in both belemnites and brachiopods, and a sharp change to an increasing trend (average $\delta^{13}C$ value in belemnites ≈ 1.38‰; average $\delta^{13}C$ value in brachiopods ≈ 1.25‰).

8. Discussion: controls in sedimentation

The interpretation and comparison of the data obtained from facies, high-order sequences, and O and C stable isotope analyses allow us to decipher controls on sedimentation, i.e. climate and internal (basin-scale) factors at the late Pliensbachian-early Toarcian in the Iberian Basin (Fig. 11).

8.1. Stable isotopes and climatic imprint

The O and C isotope curves obtained from belemnites show an increasing $\delta^{18}O$ trend and a slightly decreasing $\delta^{13}C$ trend through the *Spinatum* Zone, and subsequent opposite trends through the early Toarcian.

Interpreting the belemnite $\delta^{18}O$ values in a conservative way, i.e. as proxies for estimating seawater temperatures and/or freshwater supply in surface or intermediate seawaters (e.g. Surge *et al*., 2001; Rosales *et al*., 2004), the increasing $\delta^{18}O$ trend recorded by belemnites in the *Spinatum* Zone could be taken to reflect the cooling interlude with polar ice cap formation proposed for this time interval (Price, 1999; Dera *et al.*, 2009b, 2011, and references therein). However, this is not observed in the signal from brachiopods, which present lower $\delta^{18}O$ values and do not show any significant vertical trend. These differences could be explained by a combined effect of cooler climate and semiarid conditions, which may have amplified the ^{18}O enrichment in the sea surface. In the context of the relatively shallow areas within the epeiric platform that developed in the Iberian Basin, with a presumably reduced seawater exchange with open oceanic waters, the $\delta^{18}O$ belemnite signal would provide a more accurate record of these climate conditions (i.e. cooling and dry, semiarid conditions) than the $\delta^{18}O$ brachiopod signal. On the basis of a compilation of clay minerals data from several basins in Western Europe, Dera *et al*. (2009a) propose a distribution of palaeoclimatic belts in which the Iberian Basin would be located in a semiarid climatic belt during the Pliensbachian, therefore supporting the occurrence of dry conditions with a restricted input of freshwater in this basin. However, the palaeolatitude assumed by Dera *et al*. (2009a) (~25ºN) do not match with the values given by Osete *et al*. (2011) (~30-35ºN). Although the palaeogeographic

position proposed for the Iberian Basin is located near tropical latitudes, the observed fossil assemblages are characteristic of cool waters (foramol assemblage: molluscs, brachiopods, echinoderms, etc.) as opposed to corals or sponges, which are characteristic of tropical warm waters (Lees, 1975).

As regards the $\delta^{13}C$ record, the slightly decreasing trend of the $\delta^{13}C$ values recorded in both belemnites and brachiopods in conjunction with an increasing $\delta^{18}O$ trend would be related with an intense organic matter oxidation releasing ^{12}C to the oceanic reservoir, which in the context of non-stratified waters favoured by the proposed cooling episode would allow the upwelling of deposited organic carbon and oxic conditions (Bordenave, 1993).

The obtained isotope values suggest a relatively cold climate period for the *Spinatum* Zone recorded in the Iberian Basin, consistent with the data from other basins (e.g., Asturian Basin: Gómez & Goy, 2011; Gómez *et al*., 2015; Basque-Cantabrian Basin: Rosales *et al*., 2004; Causses Basin: Mailliot *et al.*, 2009; Lusitanian Basin: Suan *et al*., 2010). A comparison with previous stable isotope analyses in the relatively deeper section in the Iberian area (Almonacid de la Cuba section: Comas-Rengifo *et al*., 2010) and the nearby Asturian (Gómez & Goy, 2011) and Basque-Cantabrian basins (Rosales *et al*., 2004; Quesada *et al*., 2005) indicates similar isotope values for *Spinatum* Zone (Fig.12), ranging between -0.5‰ to 2.5‰ for $\delta^{18}O$ and -0.5‰ to 2‰ for $\delta^{13}C$, and displaying coeval increasing and decreasing trends respectively.

Concerning the earliest Toarcian, its sedimentary record in the studied area is limited due to sedimentary hiatuses found in the lower *Tenuicostatum* Zone and in the lower *Serpentinum* Zone, related to the sedimentary discontinuities D2 and D3, respectively. The sedimentary hiatus observed in the lowermost Toarcian, following the uppermost Pliensbachian cooling interlude, is coherent with the presence of hiatus or condensation levels described for warming episodes following cooling intervals (Morard *et al*., 2003). The lower values and general decreasing trend in $\delta^{18}O$ obtained in the early Toarcian could be indicative of the warming climate interval in the

Serpentinum Zone reported by several authors for the Iberian Basin (Gomez & Goy, 2011) and other nearby basins in Spain and Western Europe (McArthur *et al*., 2000; Röhl *et al*., 2001; Jenkyns, 2003; Rosales *et al*., 2004; Metodiev & Koleva-Rekalova, 2008; Dera *et al*., 2009b, 2011; Suan *et al*., 2010). It is important to notice that obtained $\delta^{18}O$ value corresponding to upper *Tenuicostatum* Zone is similar to those recorded in the underlying levels of the upper *Spinatum* (uppermost Pliensbachian), while obtained *Serpentinum* data show the lowest values, in concordance to the warming episode span time.

The early Toarcian warming event has been widely recognized at a global scale (e.g. Dera *et al*., 2011; Holz, 2015), associated with a major extinction among marine genera and species at the *Tenuicostatum-Serpentinum* zones boundary (Gómez &Goy, 2011; Caruthers *et al*., 2013), which has been related to the volcanic activity of the Karoo-Ferrar continental flood basalts dated to 183 ± 2 Ma (Palfy & Smith, 2000). In the context of an epeiric platform located in a semiarid climate belt, the isotope record of this warming episode would be diminished by the excess of evaporation that tends to increase the $\delta^{18}O$ of seawater, as recorded by the only slightly decreasing $\delta^{18}O$ values observed during the early Toarcian in Obón. The incomplete sedimentary record in the Obón section and the scarcity of isotope data do not allow discussing in further depth the imprint of the Toarcian warming event in the studied relatively shallow ramp areas in the Iberian Basin.

In some deeper-water successions around the world the early Toarcian warming event records widespread marine anoxia, which led to high rates of organic carbon preservation on the sea bottom and gave rise to the synchronous deposition of black-shale facies (i.e. the early Toarcian oceanic anoxic event; Jenkyns, 1988). In the relatively shallow marine domains of the Iberian Basin represented by the section studied at Obón, black-shale deposits are not recorded.

8.2. Long-term facies evolution and significance of the major discontinuities

The late Pliensbachian cooling event proposed by different authors to be linked with polar ice cap formation at high latitudes (Bailey *et al*., 2003; Rosales *et al*., 2004; Mailliot *et al.*, 2009; Suan *et al*., 2010; Gómez & Goy, 2011; Sandoval *et al*., 2012; Gómez *et al*., 2015) would result in sea-level fall and the widespread setting of upper Pliensbachian regressive successions as recorded in the Iberian Basin in the grain-supported bioclastic limestones of the Barahona Formation.

The facies and high-order sequences recorded in the study area reflect a long-term shallowing trend from *Margaritatus* Zone, up to the middle part of the *Spinatum* Zone (Fig. 11)), with the relatively deeper domains located in the more northern areas (San Pedro section; see Fig. 8).

However, even though the whole *Spinatum* Zone records the cooling episode (increasing $\delta^{18}O$ values), the shallowing-upward trend potentially linked to this cooling is interrupted within the upper *Spinatum* Zone by the discontinuity D1 related to a significant flooding event and facies polarity change, with the deeper facies located in the southern locality of Obón (see also Fig. 8). However, this sedimentary change does not have any coeval change in isotope trends (Fig. 11). So, this event can thus be taken to reflect regional (basin-scale) tectonic factors, probably due to differential subsidence recorded in other areas of the Iberian Basin (Gómez & Goy, 2000), rather than a climate control.

The discontinuity D1 has also been recognized in the relatively deeper section of Almonacid de la Cuba (Comas-Rengifo *et al*., 1999) where the associated intra-*Spinatum* transgressive event (*Apyrenym-Hawkerense* subzones boundary) represents the lithological boundary between Barahona Formation and the deeper facies (i.e., matrix-supported limestones and marls) of the overlying Turmiel Formation. In Obón, the lithological boundary between the Barahona and Turmiel formations is located above the transgressive episode coinciding with the Pliensbachian-Toarcian boundary (Fig. 11). Therefore, the different chronostratigraphic position of the lithological boundary corroborates the lateral facies relationship in concordance with the ramp polarity (i.e. deeper domains to the North). In addition, a T-R facies cycle boundary coeval to the D1

discontinuity defined in Obón was proposed in the nearby Basque-Cantabrian Basin (Fig. 13; Quesada *et al*., 2005).

D1 and D2 discontinuity surfaces bound the deepening-shallowing sequence B13-B16 (Fig. 11). The discontinuity D2 found located at the Pliensbachian-Toarcian boundary is time-equivalent to that was proposed to have a widespread significance at the third-order scale across the Iberian Basin (Fig. 13; boundary between T-R LJ3-2 and LJ3-3 sequences of Gómez & Goy, 2005). Therefore, in the shallow domains of the Iberian Basin (i.e. Obón section) the identified intra-*Spinatum* surface D1 and Pliensbachian-Toarcian discontinuity D2 have coeval discontinuity surfaces at basin-scale. However, the reported data indicates the local tectonic influence for the development of the intra-*Spinatum* discontinuity D1, whereas the discontinuity D2 found at the Pliensbachian-Toarcian boundary would have a basin wide significance as a T-R sequence boundary (Fig. 13; boundary between T-R LJ3-2 and LJ3-3 sequences of Gómez & Goy, 2005).

The discontinuity surface D3 identified in Obón within the upper *Tenuicostatum* Zone can be tentatively related with the upper boundary of the LJ3-2 third-order sequence defined in the Iberian Basin (Fig. 13; Gómez & Goy, 2005). Following this correlation, the sedimentary condensation and/or hiatus found at the lower *Serpentinum* Zone is likely to be related to the widespread flooding event occurring all across the Iberian Basin at the onset of the LJ3-3 sequence (see also Gómez & Goy, 2000).

8.3. Possible imprint of the late Pliensbachian orbital eccentricity cycles

In Obon, the long-term shallowing stage located from the upper *Margaritatus* Zone up to the intra-*Spinatum* discontinuity D1 includes 12 higher-order sequences (bundles B1–B12), which are in turn arranged in 3 lower-order deepening-shallowing sequences (sets B1-B4, B5-B8 and B9-B12; Fig.13). The interval located between discontinuities D1 and D2, in the upper part of the *Spinatum*

Zone includes 4 high-order sequences (bundles B13 to B16), which are grouped in a lower-order deepening-shallowing sequence (set of bundles B13–B16). The defined high-frequency sequences were satisfactorily correlated between the two 15-km distant studied sections (Fig. 8). The possible orbital influence in the origin of these sequences is discussed here considering the possible correlation to other upper Pliensbachian successions.

In the nearby section of Almonacid de la Cuba sedimentological and sequential work performed by Comas-Rengifo *et al*. (1999) resulted in the identification of 5 sets of sequences in the upper Pliensbachian (L, M, N, O and P; Fig. 13). The precise ammonite biostratigraphy allowed the assignment of sets of sequences L and M to the *Margaritatus* Zone, set N to *Margaritatus* and *Spinatum* zone transition, and sets O and P to the *Spinatum* Zone. These sets of sequences are comparable in terms of thickness, lithology and vertical facies evolution to the sets of bundles defined in Obón.

Considering the age calibration proposed for the Obón section (Fig. 11), a tentative correlation with the Almonacid de la Cuba is proposed (Fig.13). Accordingly, the lower set B1–B4 would correspond to set of sequences M in the upper *Margaritatus* Zone, whereas sets B5-B8, B9-B12 and B13–B16 would correlate with sets of sequences N, O and P developed during the entire *Spinatum* Zone.

It is interesting to notice that Ruhl *et al*. (2016) proposed the existence of 3 long-term (c. 400 ky) eccentricity cycles for the *Spinatum* Zone (Fig. 13).The temporal calibration for the *Spinatum* Zone (1.4 M, Gradstein *et al*., 2012) fits well this recent proposal by Ruhl *et al*. (2016). Therefore, the 3 defined sets of bundles in the *Spinatum* Zone in Obón and 3 sets of sequences in Almonacid de la Cuba would be assigned to c. 400 ky eccentricity cycles. In addition, the sets of bundles identified in Obón are each one composed by 4 bundles, which could be assigned to short-term eccentricity Milankovitch cycles (i.e., the 100 ky cycle). It is therefore suggested that the bundles

and sets of bundles defined in the Obón-San Pedro section were influenced by the short- and long-term eccentricity cycle respectively.

In the context of a storm-dominated carbonate ramp and cool climate (with the probable formation of polar ice caps), the recorded high-frequency sequences in the *Spinatum* Zone, would be probably linked to climate-induced sea-level oscillations controlling carbonate production (benthic factory) and resedimentation towards the distal areas. Similar climate control on carbonate production and resedimentation has been proposed for Milankovitch-scale high-order sequences recognized in other storm-dominated carbonate (distal middle to outer) ramp deposits of the lower Pliensbachian (Sequero *et al.*, 2017) and upper Kimmeridgian (Bádenas *et al.*, 2005 ; Colombié *et al.* 2014) of the Iberian Basin. In the studied case, the possible climate-driven high-frequency cycles (bundles and sets of bundles) have been recognized in relatively shallow (middle ramp to proximal outer ramp) deposits, a platform zone where the obliteration of the climate signal in the sedimentary record due to the imprint of the hydrodinamic agents would be expected. However, this was not the case of the studied ramp deposits, where the boundaries of both bundles and sets of bundles are prominent bedding surfaces, probably linked to a sharp decrease in carbonate production and resedimentation. However, these hydrodinamic agents actually obliterate the expected facies trends (i.e., transgressive-regressive) in the case of bundles (c.100 ky cycles), as reflected by the record of erosive events detected at bed scale within the identified bundles (see Fig. 6C).

9. Conclusions

The late Pliensbachian cooling event (*Spinatum* Zone) has been detected for first time in the relatively shallow carbonate ramp successions (proximal middle to proximal outer domains) in the Iberian Basin. The mid-ramp domain is characterized by the widespread presence of skeletal grain-supported facies, a result of both *in situ* production and the resedimentation generated after the

episodic influence of storm-induced waves. These facies grade distally to the proximal outer-ramp domain to progressively muddier sediments.

The cooling climate episode, which lasted through the *Margaritatus* p.p. Zone and the entire *Spinatum* Zone, is indicated by the increasing $\delta^{18}O$ values in belemnites. However, the facies and cyclostratigraphic analyses reflect a long-term regressive facies trend lasting through the *Margaritatus* p.p. and the upper *Spinatum* zones, followed by a sharp transgressive event at the end of the *Spinatum* Zone. The abrupt facies deepening is coeval to a change in the polarity of the carbonate ramp. Therefore, the recorded sedimentary trends do not exactly match with the cooling episode, reflecting the tectonic imprint in the upper part of the *Spinatum* Zone in the studied area. The recorded discrepancy between the facies trend and the climate-induced sea-level drop linked to the late Pliensbachian cooling event contrasts with the fitting between regression and cooling described in coeval deeper marine successions in other basins in the western Tethys. Therefore, a cooling climate episode is not always recorded as a purely shallowing facies succession, because regional or global tectonics can also control the sedimentary evolution.

The cyclostratigraphic analysis resulted in the identification of two orders of high-order sequences (bundles and sets of bundles), which were probably originated by sea-level variations induced by climatic changes in tune with the short- and long- term eccentricity Milankovitch cycles respectively. In the cold climatic context, these eustatic cycles controlled shallow production and its resedimentation towards distal zones. Even in the context of a relatively shallow storm-dominated carbonate ramp, internal factors such as reduced sedimentary rates, resedimentation and reworking, amalgamation of beds, and erosion by storm-induced currents the sedimentary signal of the climatic cycles was not completely disturbed.

Acknowledgements

This work was supported by the project CGL2014-53548-P subsidized by the Spanish Ministry of Science and Innovation, the European Regional Development Fund, the project H54 of the Government of Aragón ('Grupos Consolidados' and 'Dirección General de Patrimonio Cultural') and a Postgraduate Grant of the IAS. We are grateful to the staff of the IGME laboratories for the elemental analyses, to the staff of the laboratory of Geocronología y Geoquímica Isotópica (Universidad Complutense de Madrid) for the strontium isotopes, and to the staff of the Servicio General de Análisis de Isótopos Estables (Universidad de Salamanca) for the stable isotope analyses. We thank Rupert Glasgow for the revision of the English grammar. Authors want to acknowledge comments and suggestions from André Strasser and one anonymous reviewer, which greatly improved the preliminary version of the manuscript.

References

Alberti, M., Fürsich, F.T., Pandey, D.K. & Ramkumar, M. (2012). Stable isotope analyses of belemnites from the Kachchh Basin, western India: paleoclimatic implications for the Middle to Late Jurassic transition. *Facies* 58, 261–278.

Armendáriz, M., Rosales, I., Bádenas, B., Aurell, M., García-Ramos, J.C. & Piñuela, L. (2012). High-resolution chemostratigraphic records from Lower Pliensbachian belemnites: Palaeoclimatic perturbations, organic facies and water mass exchange (Asturian basin, northern Spain). *Palaeogeography, Palaeoclimatology, Palaeoecology* 333-334, 178-191.

Aurell, M., Robles, S., Bádenas, B., Quesada, S., Rosales, I., Meléndez, G. & García Ramos, J.C. (2003). Transgressive-Regressive Cycles and Jurassic Palaeogeography of Northeast Iberia. *Sedimentary Geology* 162, 239-271.

Bádenas, B., Aurell, M. & Gröcke, D.R. (2005). Facies analysis and correlation of high-order sequences in middle-outer ramp successions: variations in exported carbonate in basin-wide δ13Ccarb (Kimmeridgian, NE Spain). *Sedimentology* 52, 1253-1276.

Bailey, T., Rosenthal, Y., McArthur, J., van de Schootbrugge, B. & Thirlwall, M. (2003). Paleoceanographic changes of the Late Pliensbachian-Early Toarcian interval: a posible link to the genesis of an Oceanic Anoxic Event. *Earth and Planetary Science Letters* 212, 307-320.

Benito, M.I., Reolid, M. & Viedma, C. (2016). On the microstructure, growth pattern and original porosity of belemnite rostra: insight from calcitic Jurassic belemnites. *Journal of Iberian Geology* 42 (2), 201-226.

Bordenave, M.L. (1993). *Applied Petroleum Geochemistry*. Éditions Technip, 531pp.

Bordonaba, M.P. & Aurell, M. (2002). El Pliensbachiense de la Rama Aragonesa de la Cordillera Ibérica: Análisis de facies y establecimiento de secuencias. *Cuadernos de Geología Ibérica* 28, 31-44.

Brand, U., Logan, A., Hiller, N. & Richardson, J. (2003). Geochemistry of modern brachiopods: applications and implications for oceanography and palaeoceanography. *Chemical Geology* 198, 305-334.

Burchette, T.P. & Wright, V.P. (1992). Carbonate ramp and deposition. *Sedimentary Geology* 79, 3-57.

Burke, W., Denison, R., Hetherington, E., Koepnick, R., Nelson, H. & Otto, J. (1982). Variation of $^{87}Sr/^{86}Sr$ throughout Phanerozoic time. *Geology* 10, 516-519.

Carpenter, S.J. & Lohmann, K.C. (1995). δ18O and δ13C values of modern brachiopod valves. *Geochimica et Cosmochimica Acta* 59, 3749-3764.

Caruthers, A., Smith, P. & Gröcke, D. (2013). The Pliensbachian-Toarcian (Early Jurassic) extinction, a global multi-phased event. *Palaeogeography, Palaeoclimatology, Palaeoecology* 386, 104-118.

Colombié, C., Lécuyer, C. & Strasser, A. (2011). Carbon- and oxygen-isotope records of palaeoenvironmental and carbonate production changes in shallow-marine carbonates (Kimmeridgian, Swiss Jura). *Geological Magazine* 148, 133-153.

Colombié, C., Bádenas, B., Aurell, M., Götz, A., Bertholon, S. & Boussaha, M. (2014). Feature and duration of metre-scale sequences in a storm-dominated carbonate ramp setting (Kimmeridgian, northeastern Spain). *Sedimentary Geology* 312, 94-108.

Comas-Rengifo, M.J., Gómez, J.J., Goy, A., Herrero, C., Perilli, N. & Rodrigo, A. (1999). El Jurásico Inferior en la sección de Almonacid de la Cuba (sector central de la Cordillera Ibérica, Zaragoza, España). *Cuadernos de Geología Ibérica* 25, 27-57.

Comas-Rengifo, M.J., Gómez, J.J., Goy, A., Osete, M.L. & Palencia-Ortas, A. (2010). The base of the Toarcian (Early Jurassic) in the Almonacid de la Cuba section (Spain). Ammonite biostratigraphy, magnetostratigraphy and isotope stratigraphy. *Episodes* 33, 15-22.

Dera, G., Pellenard, P., Neige, P., Deconinck, J., Pucéat, E. & Dommergues, J. (2009a). Distribution of clay minerals in Early Jurassic Perithethyan seas: Palaeoclimatic significance inferred from multiproxy comparisons. *Palaeogeography, Palaeoclimatology, Palaeoecology* 271, 39-51.

Dera, G., Pucéat, E., Pellenard, P., Neige, P., Delsate, D., Joachimski, M., Reisberg, L. & Martinez, M. (2009b). Water mass exchange and variations in seawater temperature in the NW Tethys during the Early Jurassic: evidence from neodymium and oxygen isotopes of fish teeth and belemnites. *Earth Planet Science Letters* 286, 198-207.

Dera, G., Brigaud, B., Monna, F., Laffont, R., Pucéat, E., Deconinck, J.F., Pellenard, P., Joachimski, M.M. & Durlet, C. (2011). Climatic ups and downs in a disturbed Jurassic world. *Geology* 39, 215-218.

Fan, S., Swift, D.J.P., Traykovski, P., Bentley, S., Borgeld, J.C., Reed, C.W., Niedoroda, A.W. (2004). River flooding, storm resuspension, and event stratigraphy on the northern California shelf: observations compared with simulations. *Marine Geology* 210, 17–41.

Gómez, J.J. & Goy, A. (2000). Definition and organization of limestone-marl cycles in the Toarcian of the northern and east-central part of the Iberian Subplate (Spain). In: Hall, R.L., Smith, P.L. (Eds.), Advances in Jurassic Research 2000. *GeoResearch Forum,* vol. 6, 301-310.

Gómez, J.J. & Goy, A. (2005). Late Triassic and Early Jurassic palaeogeographic evolution and depositional cycles of the Western Tethys Iberian platform system (Eastern Spain). *Palaeogeography, Palaeoclimatology, Palaeoecology* 222, 77-94.

Gómez, J.J. & Goy, A. (2011). Warming-driven mass extinction in the Early Toarcian (Early Jurassic) of northern and central Spain. Correlation with other time-equivalent European sections. *Palaeogeography, Palaeoclimatology, Palaeoecology* 306, 176-195.

Gómez, J.J., Comas-Rengifo, M.J. & Goy, A. (2015). Palaeoclimatic oscillations in the Pliensbachian (Lower Jurassic) of the Asturian Basin (Northern Basin). *Climate of the Past Discussions* 11, 4039-4076.

Goy, A., Gómez, J.J. & Yébenes, A. (1976). El Jurásico de la rama castellana de la Cordillera Ibérica (mitad norte): I. Unidades litoestratigráficas. *Estudios Geológicos* 32, 391-423.

Gradstein, F., Ogg, J., Schmitz, M. & Ogg, G., eds. (2012). *The geologic time scale 2012*. Boston, Elsevier, 1176pp.

Hoffmann, R., Richter, D.K., Neuser, R.D., Jöns, N., Linzmeier, B.J., Lemanis, R.E., Fusseis, F., Xiao, X. & Immenhauser, A. (2016). Evidence for a composite organic-inorganic fabric of

belemnite rostra: Implications for palaeoceanography and palaeoecology. *Palaeogeography, Palaeoclimatology, Palaeoecology* 341, 203-215.

Holz, M. (2015). Mesozoic paleogeography and paleoclimates – A discussion of the diverse greenhouse and hothouse conditions of an alien world. *Journal of South American Earth Sciences* 61, 91-107.

Jenkyns, H. (1988). The early Toarcian (Jurassic) anoxic event: stratigraphic, sedimentary and geochemical evidence. *American Journal of Science* 288, 101-151.

Jenkyns, H. (2003). Evidence for rapid climate change in the Mesozoic-Palaeogene greenhouse world. *Philosophical Transactions of the Royal Society of London A* 361, 1885-1916.

Jenkyns, H. & Clayton, C. (1997). Lower Jurassic epicontinental carbonates and mudstones from England and Wales: chemostratigraphic signals and the early Toarcian anoxic event. *Sedimentology* 44, 687-706.

Jones, C.E. & Jenkyns, H.C. (2001). Seawater strontium isotopes, oceanic anoxic events, and seafloor hydrothermal activity in the Jurassic and Cretaceous. *American Journal of Science* 301, 112–149.

Kidwell, S.M. & Holland, S.M. (1991). Field description of coarse bioclastic fabrics. *Palaios* 6, 426-434.

Lees, A. (1975). Possible influence of salinity and temperature on modern shelf carbonate sedimentation. *Marine Geology* 19, 159-198.

Mailliot, S., Mattioli, E., Bartolini, A., Baudin, F., Pittet, B. & Guex, J. (2009). Late Pliensbachian – Early Toarcian (Early Jurassic) environmental changes in an epicontinental basin of NW Europe (Causses area, central France): A micropaleontological and geochemical approach. *Palaeogeography, Palaeoclimatology, Palaeoecology* 273, 346-364.

McArthur, J., Donovan, D., Thirlwall, M., Fouke, B. & Mattey, D. (2000). Strontium isotope profile of the early Toarcian (Jurassic) oceanic anoxic event, the duration of ammonite biozones, and belemnite palaeotemperatures. *Earth Planet Science Letters* 179, 269-285.

McArthur, J.M., Doyle, P., Leng, M.J., Reeves, K., Williams, C.T., García-Sanchez, R. & Howarth, R.J. (2007). Testing palaeo-environmental proxies in Jurassic belemnites: Mg/Ca, Sr/Ca, Na/Ca, $\delta^{18}O$ and $\delta^{13}C$. *Palaeogeography, Palaeoclimatology, Palaeoecology* 252, 464-480.

McArthur, J., Steuber, T., Page, K. & Landman, N. (2016). Sr- Isotope stratigraphy: assigning time in the Campanian, Pliensbachian, Toarcian, and Valanginian. *The Journal of Geology* 124, 569-586.

Metodiev, L. & Koleva-Rekalova, E. (2008). Stable isotope records ($\delta^{18}O$ and $\delta^{13}C$) of Lower-Middle Jurassic belemnites from the Western Balkan mountains (Bulgaria): Palaeoenvironmental application. *Applied Geochemistry* 23, 2845-2856.

Metodiev, L., Savov, I., Gröcke, D., Wignall, P., Newton, R., Andreeva, P. & Koleva-Rekalova, E. (2014). Paleoenvironmental conditions recorded by $^{87}Sr/^{86}Sr$, $\delta^{13}C$ and $\delta^{18}O$ in late Pliensbachian-Toarcian (Jurassic) belemnites from Bulgaria. *Palaeogeography, Palaeoclimatology, Palaeoecology* 409, 98-113.

Morard, A., Guex, J., Bartolini, A., Morettini, E. & de Weber, P. (2003). A new scenario for the Domerian-Toarcian transition. *Bulletin de la Société géologique de France* 174, 351-356.

Morrison, J.O. & Brand, U. (1986). Geochemistry of recent marine invertebrates. *Geoscience Canana* 13, 237–254.

Mouterde, R., Fernández-López, S., Goy, A., Linares, A., Rivas, P., Ruget, C., & Suárez-Vega, L.C. (1978). El Jurásico de la región de Obón (Teruel). In: *Guía de las excursiones al Jurásico de la Cordillera Ibérica.* Grupo Español del Mesozoico 11.1-11.13.

Osete, M., L., Gómez, J.J., Pavón-Carrasco, F.J., Villalaín, J.J., Palencia-Ortas, A., Ruiz-Martínez, V.C. & Heller, F. (2011). The evolution of Iberia during the Jurassic from palaeomagnetic data. *Tectonophysics* 502, 105-120.

Palfy, J. & Smith, P. (2000). Synchrony between Early Jurassic extinction, oceanic anoxic event, and the Karoo-Ferrar flood basalt volcanism. *Geology* 28, 747-750.

Price, G. (1999). The evidence and implications of polar ice during the Mesozoic. *Earth-Science Reviews* 48, 183-210.

Quesada, S., Robles, S. & Rosales, I. (2005). Depositional architecture and transgressive-regressive cycles within Liassic backstepping carbonate ramps in the Basque-Cantabrian basin, northern Spain. *Journal of the Geological Society* 162, 531-548.

Rexfort, A. & Mutterlose, J. (2009). The role of biogeography and ecology on the isotope signature of cuttlefishes (Cephalopoda, Sepiidae) and the impact on belemnite studies. *Palaeogeography, Palaeoclimatology, Palaeoecology* 284, 153-163.

Röhl, H., Schmid-Röhl, A., Oschmann, W., Frimmel, A. & Schwark, L. (2001). The Posidonia Shale (Lower Toarcian) of SW-Germany: an oxygen-depleted ecosystem controlled by sea level and palaeoclimate. *Palaeogeography, Palaeoclimatology, Palaeoecology* 165, 27-52.

Rosales, I., Quesada, S. & Robles, S. (2001). Primary and diagenetic isotopic signals in fossils and hemipelagic carbonates: the Lower Jurassic of northern Spain. *Sedimentology* 48, 1149-1169.

Rosales, I., Quesada, S. & Robles, S. (2004). Paleotemperature variations of Early Jurassic seawater recorded in geochemical trends of belemnites from the Basque-Cantabrian basin, northern Spain. *Palaeogeography, Palaeoclimatology, Palaeoecology* 203, 253-275.

Ruhl, M., Hesselbo, S., Hinnov, L., Jenkyns, H., Xu, W., Riding, J., Storm, M., Minisini, D., Ullmann, C. & Leng, M. (2016). Astronomical constraints on the duration of the Early

Jurassic Pliensbachian Stage and global climatic fluctuations. *Earth and Planetary Science Letters* 455, 149-165.

Sandoval, J., Bill, M., Aguado, R., O'Dogherty, L., Rivas, P., Morard, A. & Guex, J. (2012). The Toarcian in the Subbetic basin (southern Spain): Bio-events (ammonite and calcareous nannofossils) and carbon-isotope stratigraphy. *Palaeogeography, Palaeoclimatology, Palaeoecology* 342, 40-63.

Sælen, G. (1989). Diagenesis and construction of the belemnite rostrum. *Paleontology* 32, 765–798.

Schwarzacher, W. (2000). Repetitions and cycles in stratigraphy. *Earth-Science Reviews* 50, 51-75.

Sequero, C., Bádenas, B. & Muñoz, A. (2017). Sedimentología y cicloestratigrafía de las calizas fangosas de plataforma abierta de la Fm. Río Palomar (Pliensbachiense inferior; Cuenca Ibérica). *Revista de la Sociedad Geológica de España* 30(1), in press.

Strasser, A., Pittet, B., Hillgärtner, H. & Pasquier, J.B. (1999). Depositional sequences in shallow carbonate-dominated sedimentary systems: concepts for a high-resolution analysis. *Sedimentary Geology* 128, 201–221.

Strasser, A., Aurell, M., Bádenas, B., Meléndez, G. & Tomás, S. (2005). From platform to basin to swell: orbital control on sedimentary sequences in the Oxfordian, Spain. *Terra Nova* 12, 407–413.

Suan, G., Mattioli, E., Pittet, B., Lécuyer, C., Suchéras-Marx, B., Duarte, L.V., Philippe, M., Reggiani, L. & Martineau, F. (2010). Secular environmental precursors to Early Toarcian (Jurassic) extreme climate changes. *Earth and Planetary Science Letters* 290, 448-458.

Surge, D., Lohmann, K.C. & Dettman, D. (2001). Controls on isotopic chemistry of the American oyster, *Crassostrea virginica*: implications form growth patterns. *Palaeogeography, Palaeoclimatology, Palaeoecology* 172, 283-296.

Taylor, A.M. & Goldring, R. (1993). Description and analysis of bioturbation and ichnofabric. *Journal of the Geological Society of London* 150, 141-148.

Ullman, C., Hesselbo, S. & Korte, C. (2013). Tectonic forcing of Early to Middle Jurassic seawater Sr/Ca. *Geology* 41: 12, 1211-1214.

Val, J. & Bádenas, B. (2014). Sedimentología y cicloestratigrafía de la Formación Barahona (Jurásico Inferior) en la Rama Aragonesa de la Cordillera Ibérica. *Geogaceta* 56, 47-50.

Wierzbowski, H. (2004). Carbon and oxygen isotope composition of Oxfordian-Early Kimmeridgian belemnite rostra: palaeoenvironmental implications for Late Jurassic seas. *Palaeogeography, Palaeoclimatology, Palaeoecology* 203, 153-168.

Wierzbowski, H. & Joachimski, M. (2007). Reconstruction of late Bajocian-Bathonian marine palaeoenvironments using carbon and oxygen isotope ratios of calcareous fossils from the Polish Jura Chain (central Poland). *Palaeogeography, Palaeoclimatology, Palaeoecology* 254, 523-540.

Figure Captions

Figure 1: A): Geographic location of the studied upper Pliensbachian Obón and San Pedro sections; the distribution of Jurassic outcrops across the Iberian Range are indicated in blue. B): Palaeogeographical context of the Iberian Basin during the Pliensbachian-Toarcian interval. Compiled from Aurell *et al*. (2003) and Armendáriz *et al*. (2013); palaeolatitude adapted from Osete *et al*. (2011). C): Chronostratigraphic distribution of the main Lower Jurassic facies across the northern Iberian Chain (Aragonese branch) indicating the studied interval within the Barahona Formation under study (modified from Aurell *et al*., 2003). The transgressive-regressive third order cycles defined in the Iberian Basin by Gómez & Goy (2005) are also shown.

Figure 2: Field view of the studied outcrops of the Barahona Formation in Obón (A) and San Pedro (B), showing the distribution of three main lithological intervals: a lower interval dominated by limestone-marl alternation; a middle interval of tabular limestones; and an upper interval of nodular limestones and marls. In both sections, the presence of well-marked plane beds allows further division of the Barahona Formation in 16 bundles of beds (B1–B16).

Figure 3: Sedimentological data, higher-order sequences (bundles of beds) and chemostratigraphic data in the Obón section. The data obtained for $\delta^{18}O$ and $\delta^{13}C$ are drawn in two different curves (i.e. data from belemnites and from brachiopods).

Figure 4: Sedimentological data and higher-order high-frequency sequences (bundles of beds) in the San Pedro section.

Figure 5: A to D): Polished slabs of the different skeletal facies of the upper Pliensbachian Barahona Formation. (A): Facies *M* (mudstones). (B): Facies *W* (wackestones). (C): Facies *fP* (fine packstones). (D): Facies *cP* (coarse packstones). E): Field view of facies *L* (lumachelle beds).

Figure 6: Different modes of vertical facies evolution in the bioclastic accumulation levels. A): Crude fining-upward trend. B): Clear fining-upward trend. C): Amalgamated levels. Facies legend: *M* (mudstones); *W* (wackestones); *fP* (fine packstones); *cP* (coarse packstones). Scale bar in cm.

Figure 7: Sedimentary model proposed for the Barahona Formation, indicating the distribution of the main facies belts and sedimentary processes from proximal middle carbonate ramp to proximal outer-ramp domains. Thin-section images in plane-polarized light of facies *cP*,

fP and *W* are also included (*cP:* coarse packstones; *fP*: fine packstones; *W*: wackestones; *M*: mudstones; *mL*: marly limestones; *m*: marls).

Figure 8: Correlation of the higher-order sequences (bundles of beds B1–B16) recognized in the Obón and San Pedro sections, which allows the lateral facies relationships to be characterized. Four lower-order sequences (sets of bundles) have been defined.

Figure 9: A): Age calibration proposed for the Obón section based on stable isotopic data ($^{87}Sr/^{86}Sr$ curve) and previous ammonite data provided by Mouterde *et al*. (1978). The first Toarcian ammonites found in level 57 correspond to the upper *Tenuicostatum* (U.T.) Zone. The Pliensbachian-Toarcian boundary was located at the top of bed 56, in the boundary between the Barahona and Turmiel formations. B): Comparison of the obtained $^{87}Sr/^{86}Sr$ data for the upper Pliensbachian– lower Toarcian of Obón with the nearby section of Almonacid de la Cuba (Comas-Rengifo *et al*., 2010), the $^{87}Sr/^{86}Sr$ values through Pliensbachian and Toarcian in the Geological Time Scale of Gradstein *et al*. (2012) and the range of $^{87}Sr/^{86}Sr$ values given by Ruhl *et al*. (2016) through *Margaritatus* and *Spinatum* zones in UK and Portugal.

Figure 10: Photomicrographs showing the degree of preservation of belemnite samples. A, B): Transmitted light microscope (TL) photographs from longitudinal sections of belemnite rostra. The belemnite rostra have a clear and translucent appearance except in the apical line that becomes cloudy. The location of more detailed pictures below is also shown. C-C'): Detailed picture under transmitted light microscope (C) and cathodoluminescence microscope (C') through the apical line shown in A. The cloudy apical line is luminescent in contrast to the rest of the belemnite rostrum, which is non-luminescent except for small microstylolite-related diagenetically altered lines. D-D'): Detailed picture under transmitted light microscope (D) and cathodoluminescence microscope (D') of the belemnite area shown in B. The well-preserved

belemnite rostrum is non-luminescent. The sediment filling the phragmocone area is orange luminescent. E-E'): Detailed picture under transmitted light microscope (E) and cathodoluminescence microscope (E') through the fibrous microstructure of the belemnite shown in A. The belemnite is largely non-luminescent except for the boundaries between some radial fibres, which have a cloudier appearance.

Figure 11: Summary of the sedimentology, cyclostratigraphy and chemostratigraphy in the Obón section, with the interpretation of the main sedimentary stages and controlling factors at the late Pliensbachian-earliest Toarcian time span (U.T.: upper *Tenuicostatum* Zone).

Figure 12: Comparison of the stable isotopic curves (A: $\delta^{18}O$; B: $\delta^{13}C$) obtained from belemnite rostra in Obón (this work) with the nearby section of Almonacid de la Cuba (Comas Rengifo *et al.*, 2010), the Asturian Basin (Gómez *et al*., 2015) and the Basque-Cantabrian Basin (Rosales *et al*., 2004; Quesada *et al.*, 2005). The dashed line delimits the *Spinatum* zone extension.

Figure 13: Proposed correlation of the major discontinuities (D1, D2 and D3, see Fig. 11) recognized in the Obón section with the boundaries of the third order cycles defined for the Iberian Basin (Gómez & Goy, 2005) and the Basque-Cantabrian Basin (Quesada *et al*., 2005). The four sets of bundles recognized in Obón have been tentatively correlated to the four sets of sequences (M–P) identified in the Almonacid de Cuba section by Comas-Rengifo (1999). It is suggested that these four sets may be time-equivalent to the 400ky cycles defined by Ruhl *et al*. (2016) for the upper *Margaritatus* and *Spinatum* zones.

Table 1: Results of stable isotope, strontium isotopes, and major and trace element analyses from 89 analyzed samples of the Obón section.

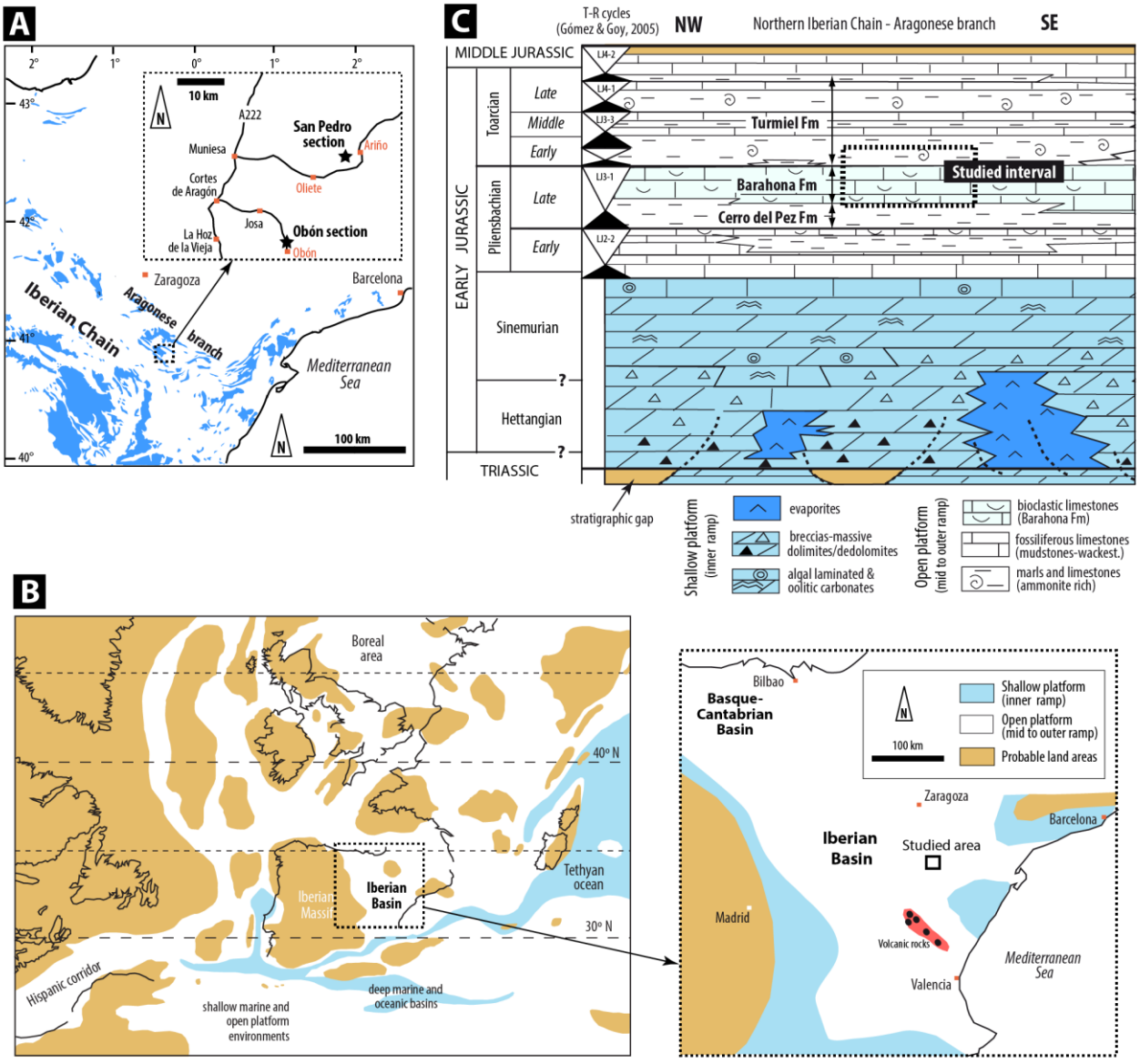

Figure 1

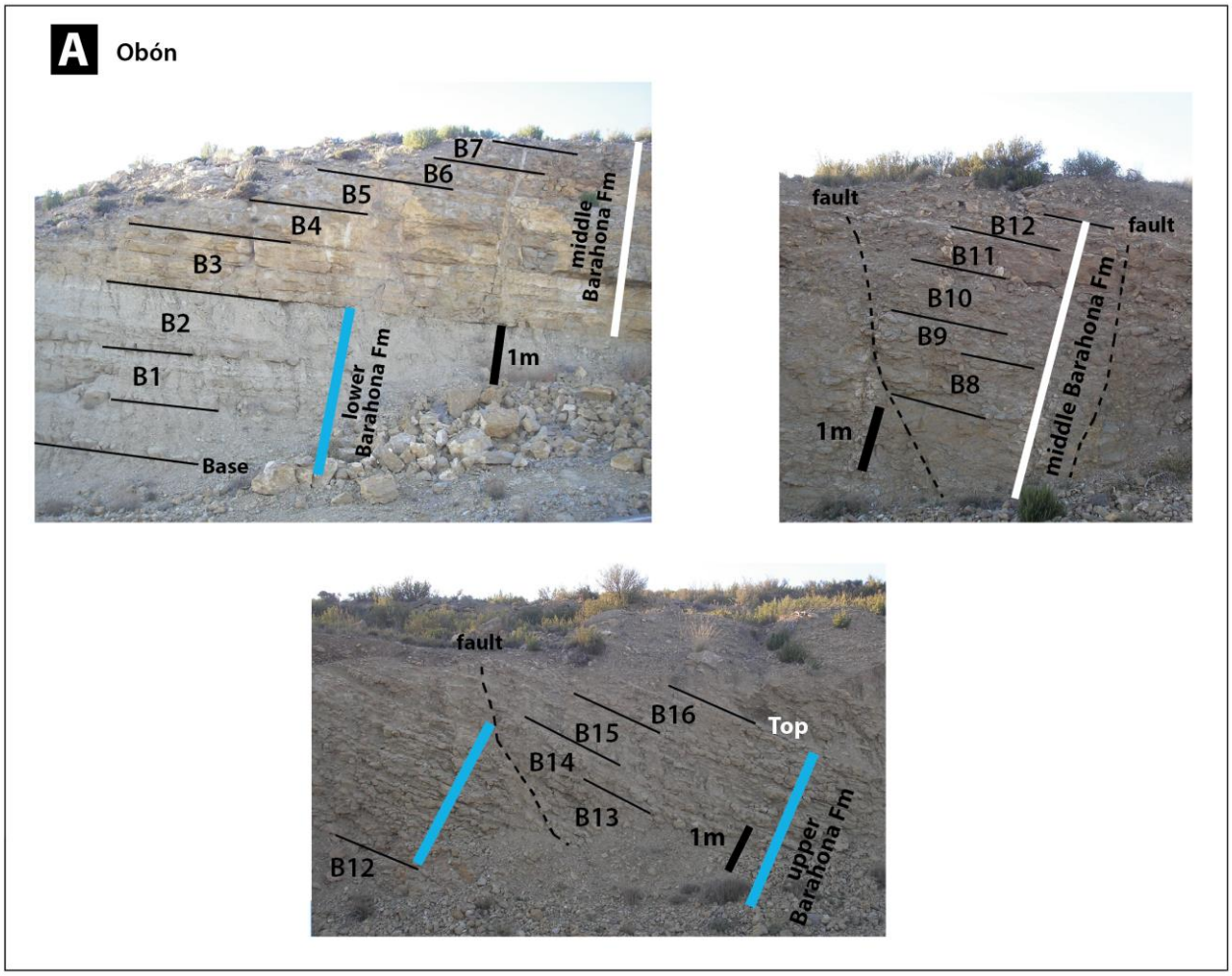

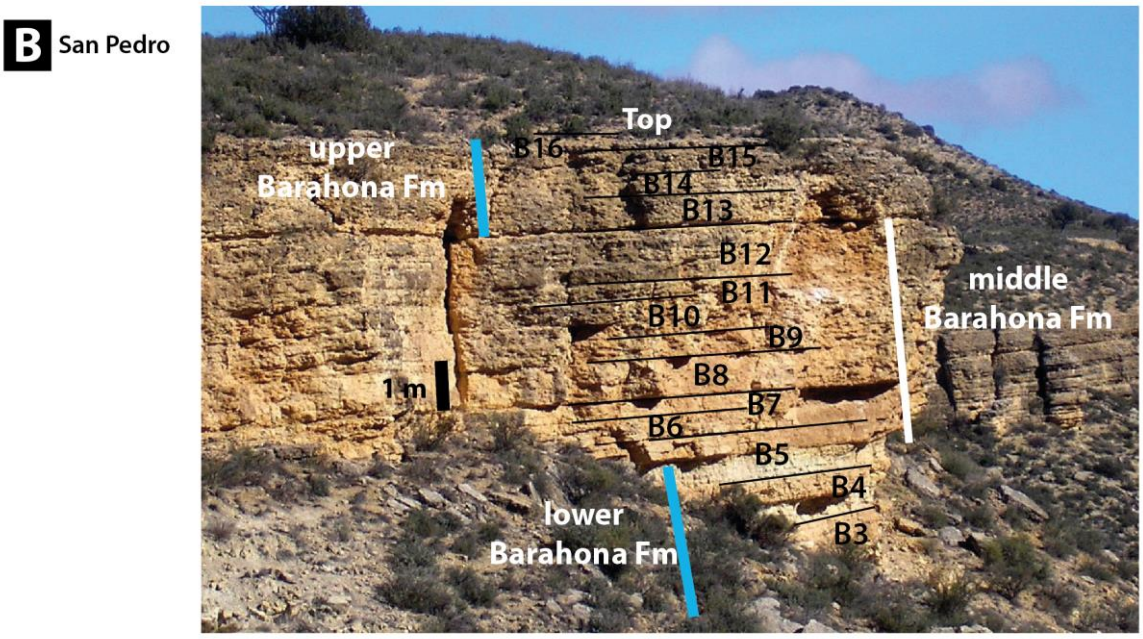

Figure 2

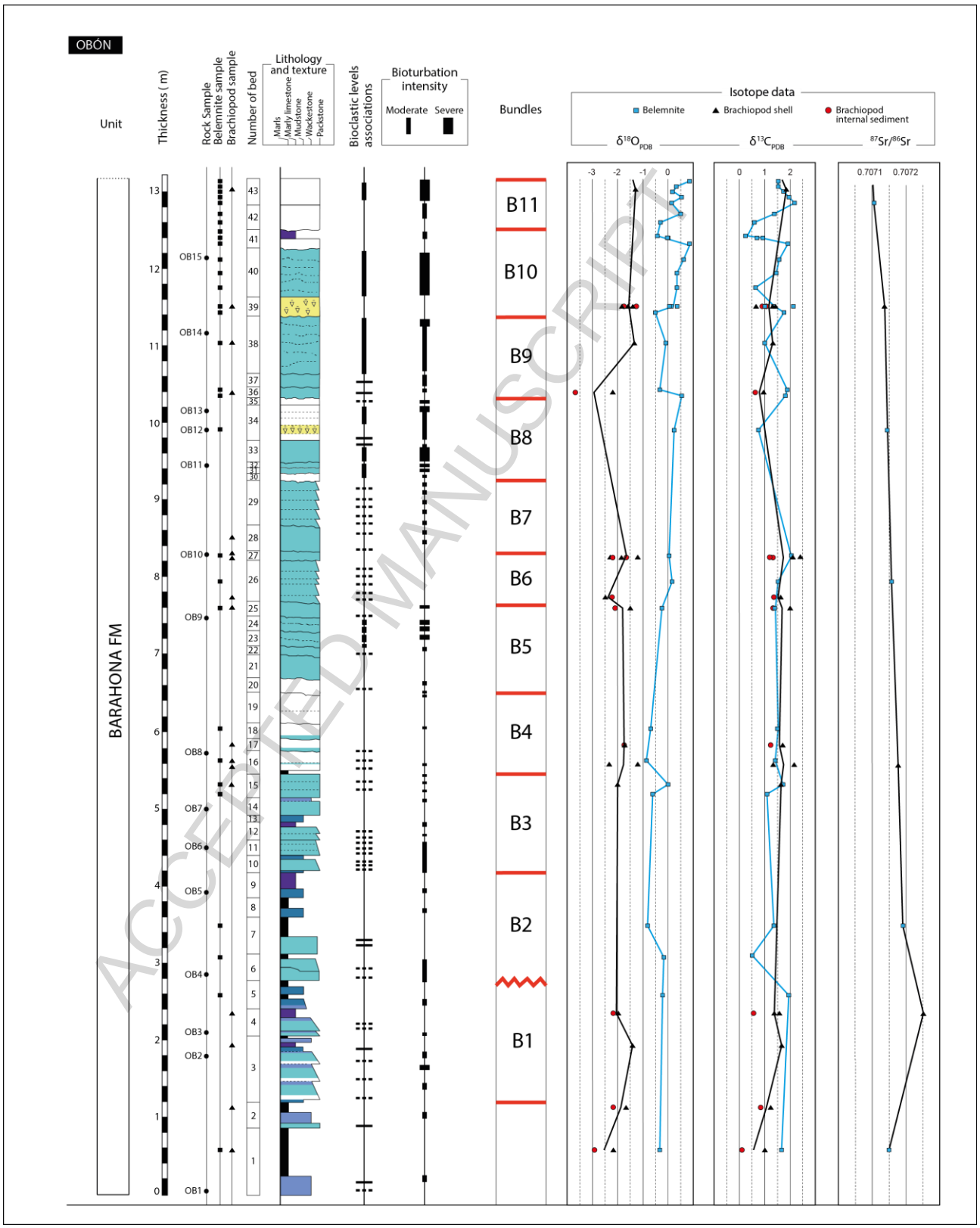

Figure 3.1

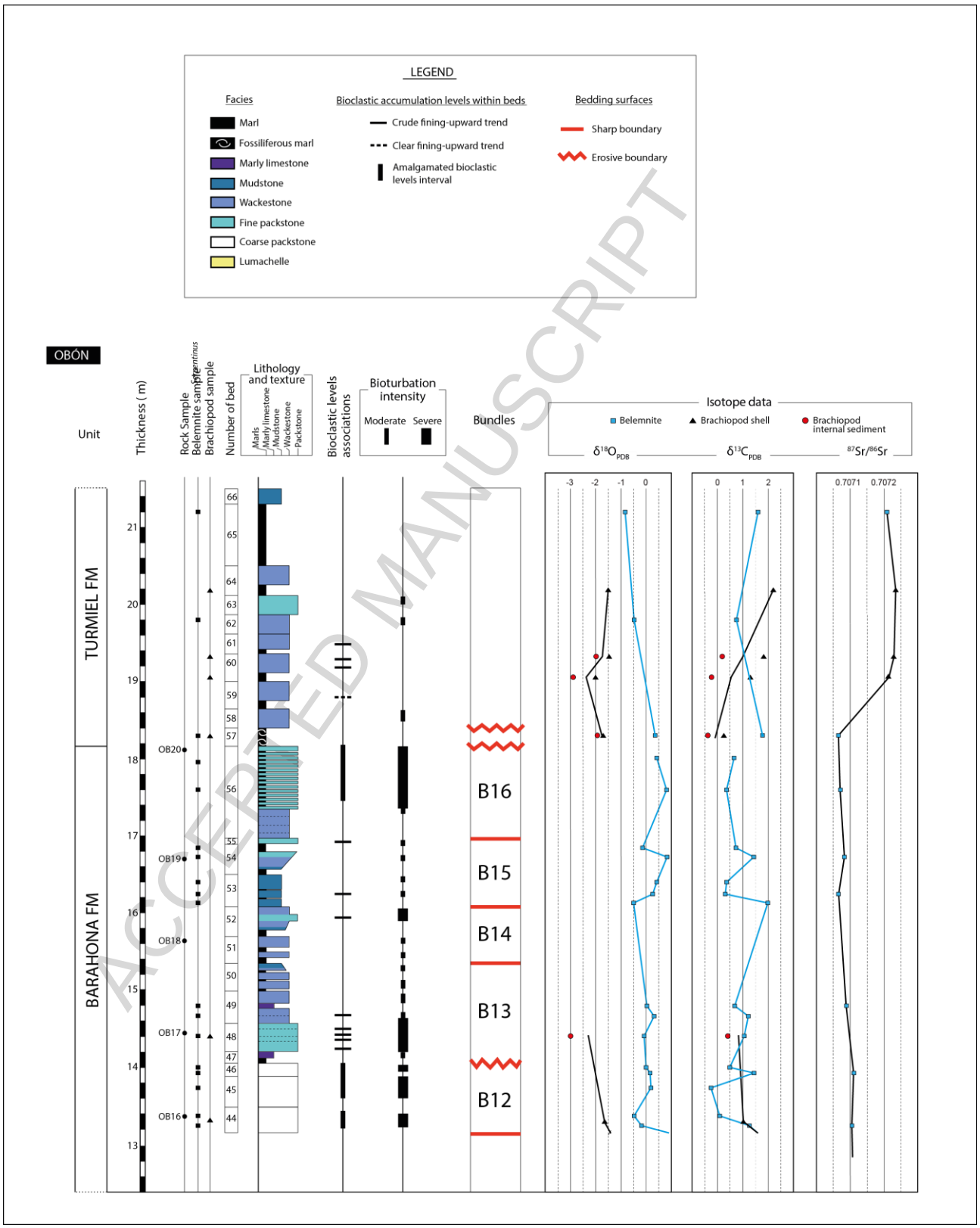

Figure 3.2

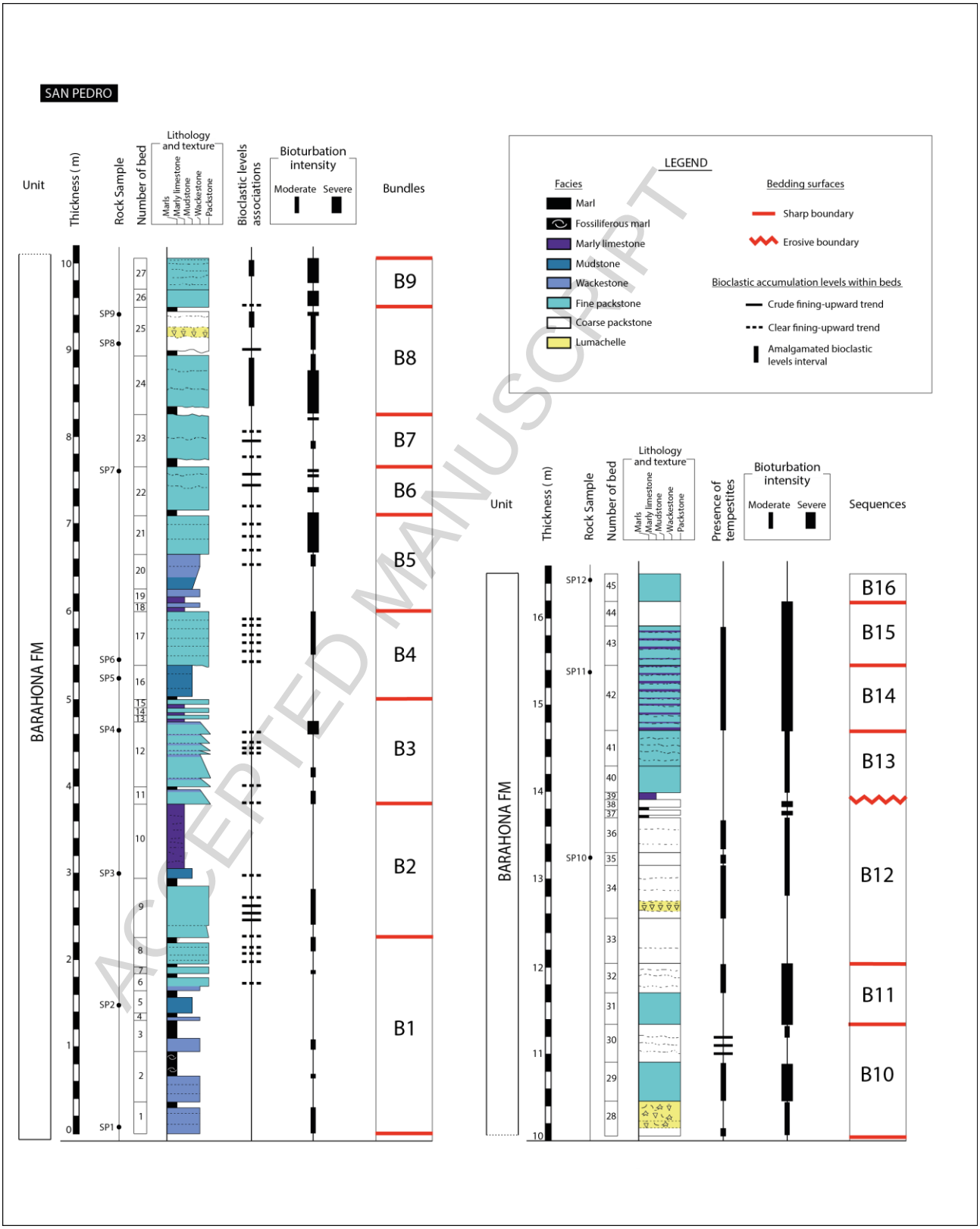

Figure 4

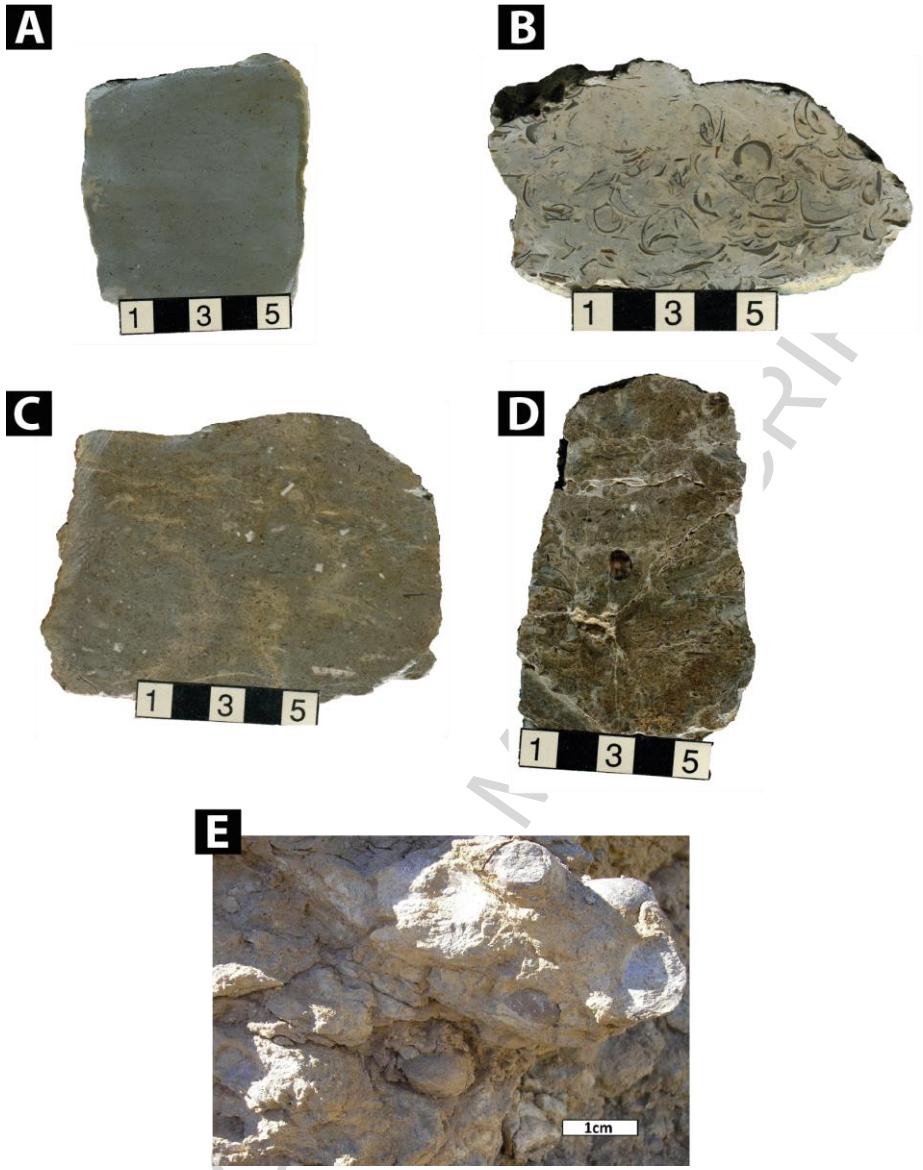

Figure 5

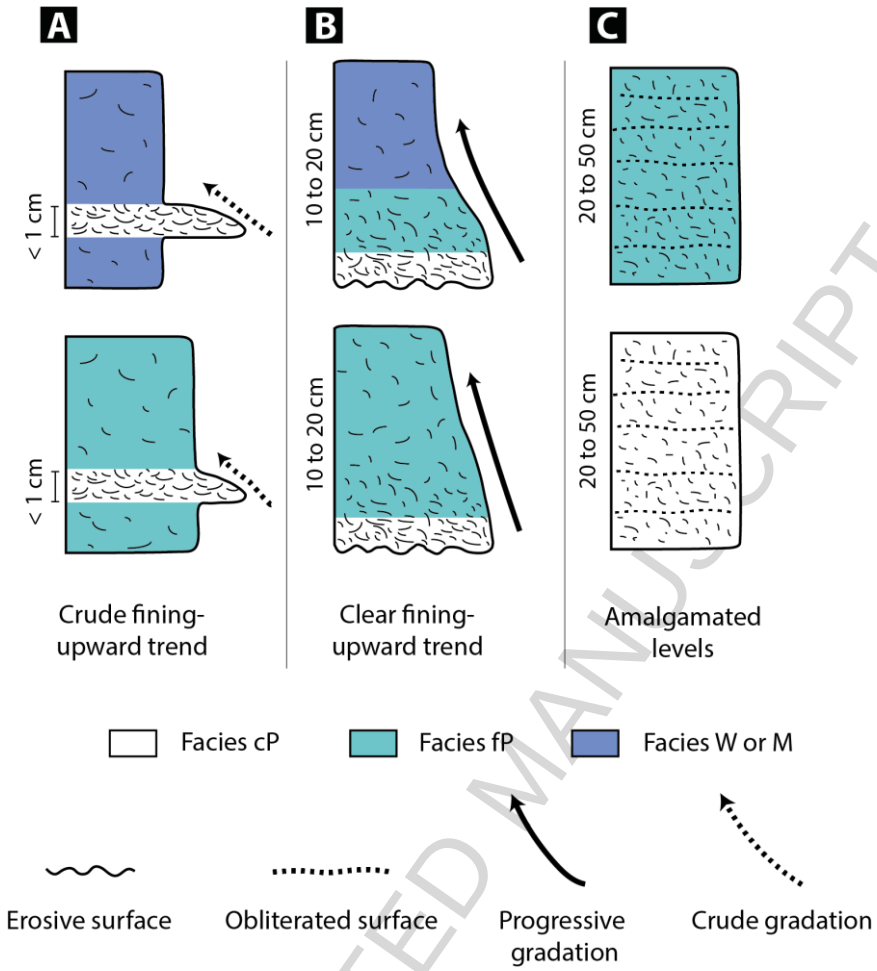

Figure 6

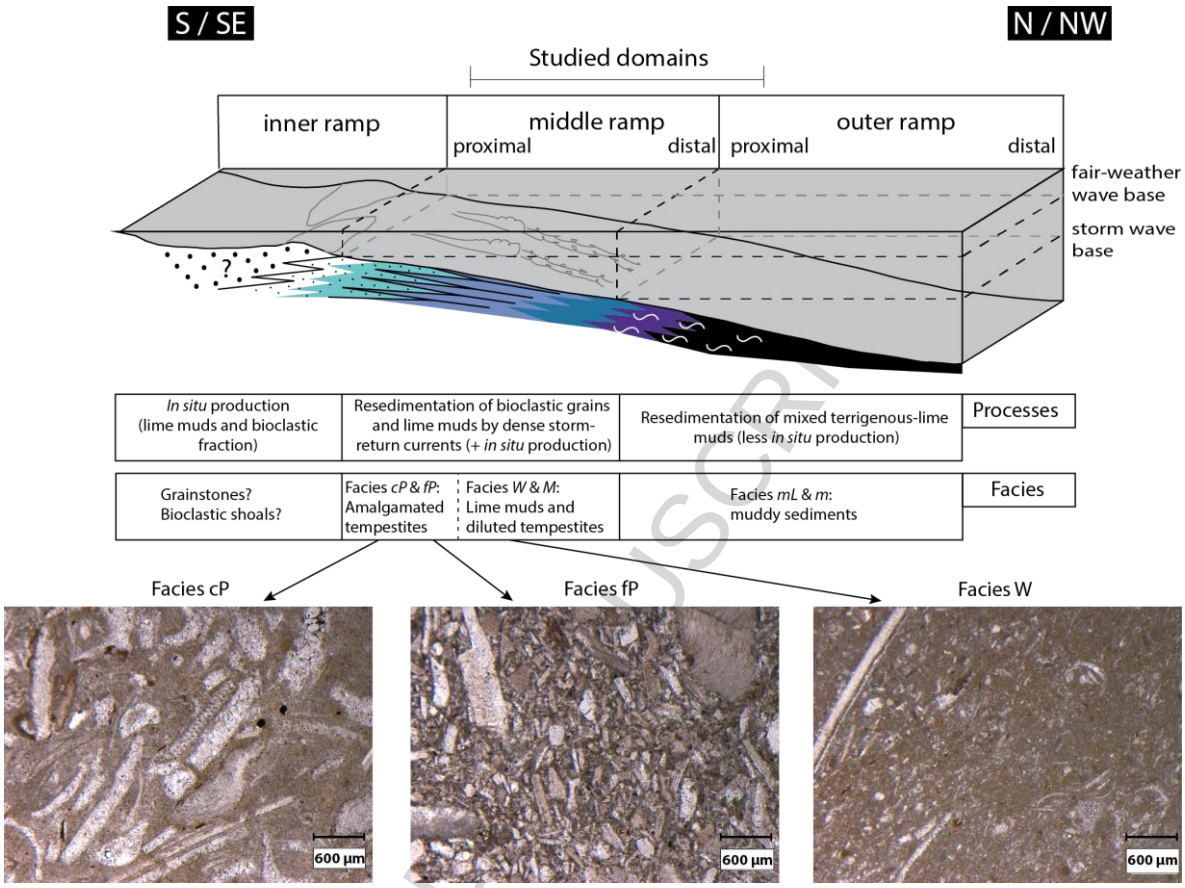

Figure 7

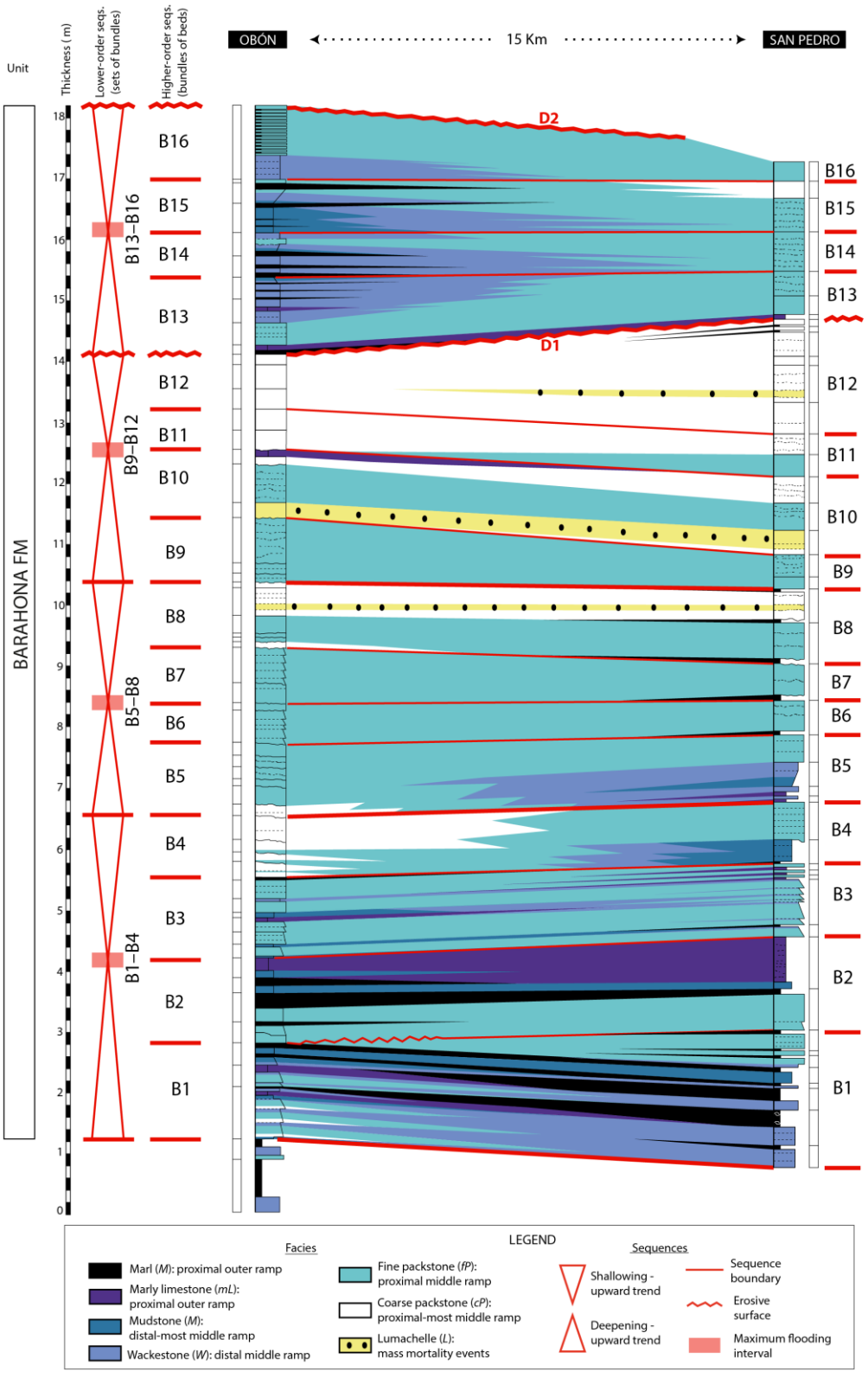

Figure 8

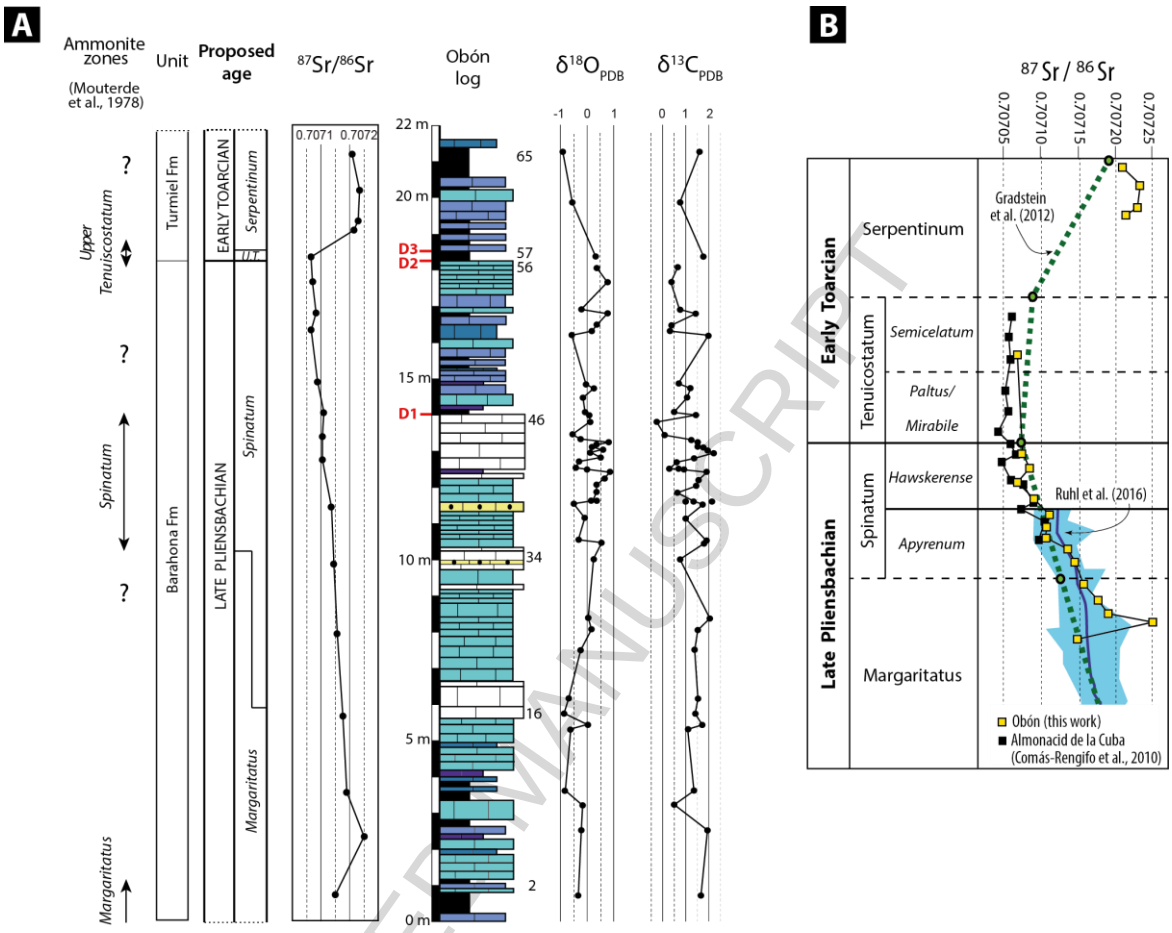

Figure 9

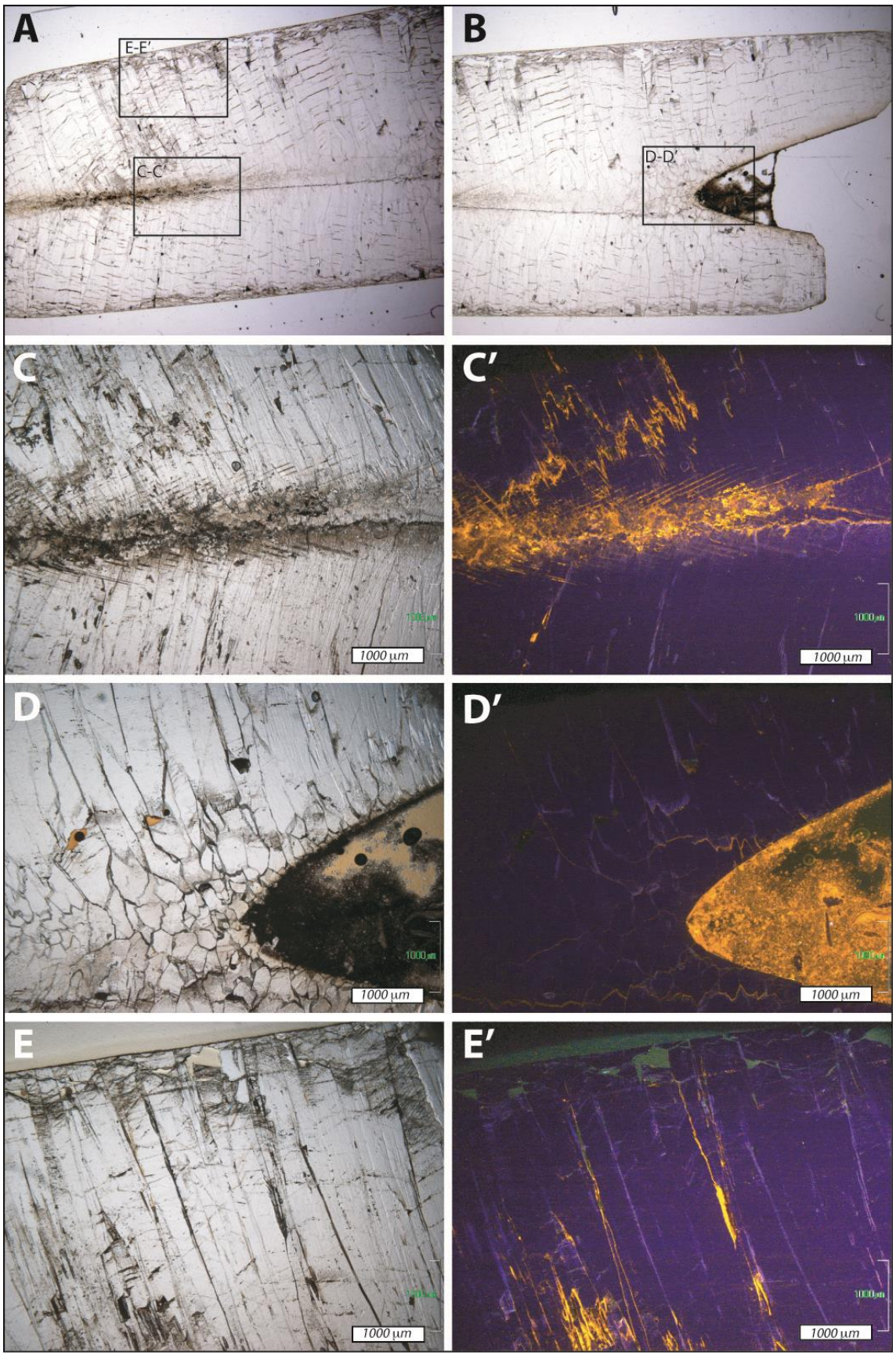

Figure 10

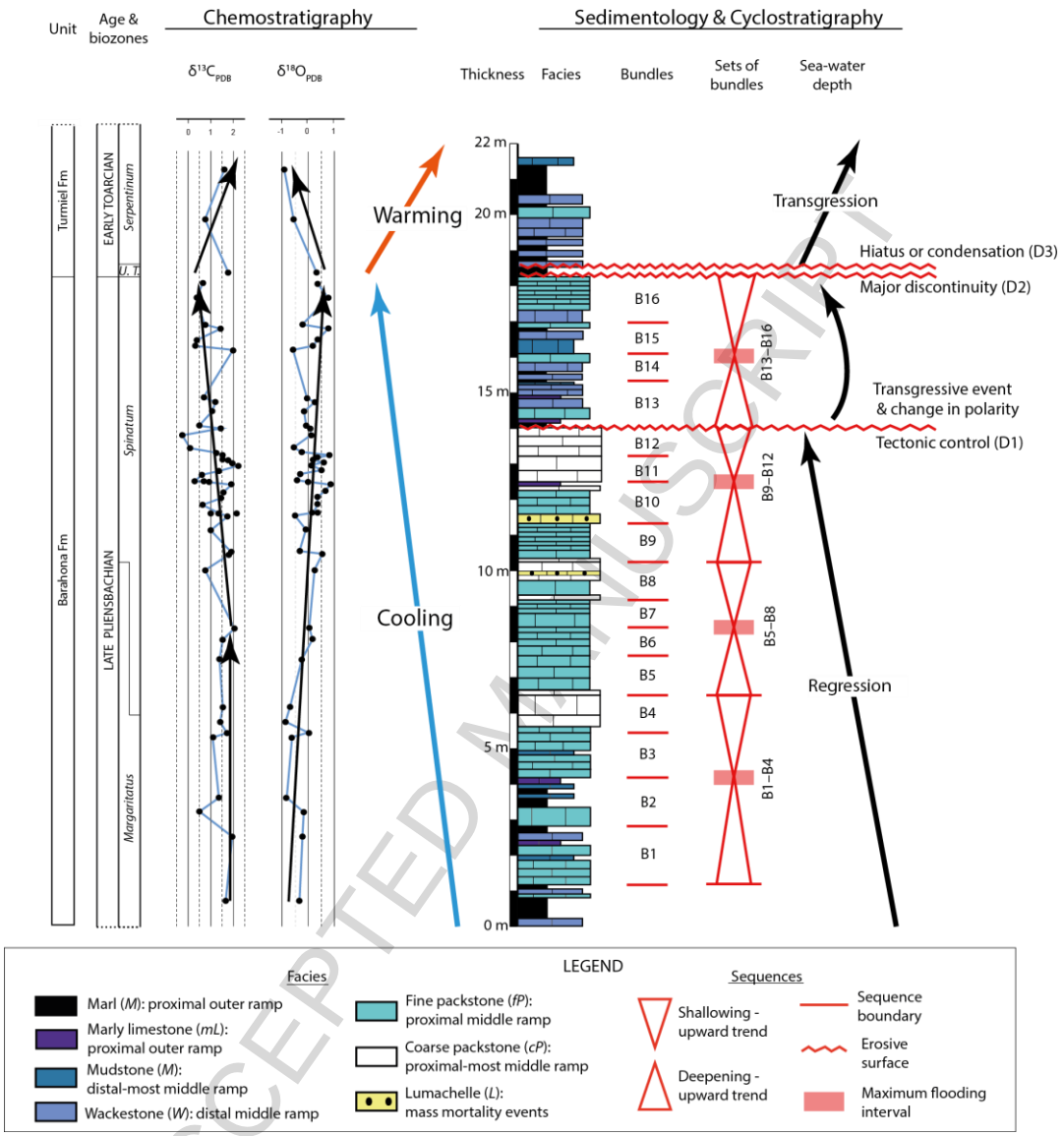

Figure 11

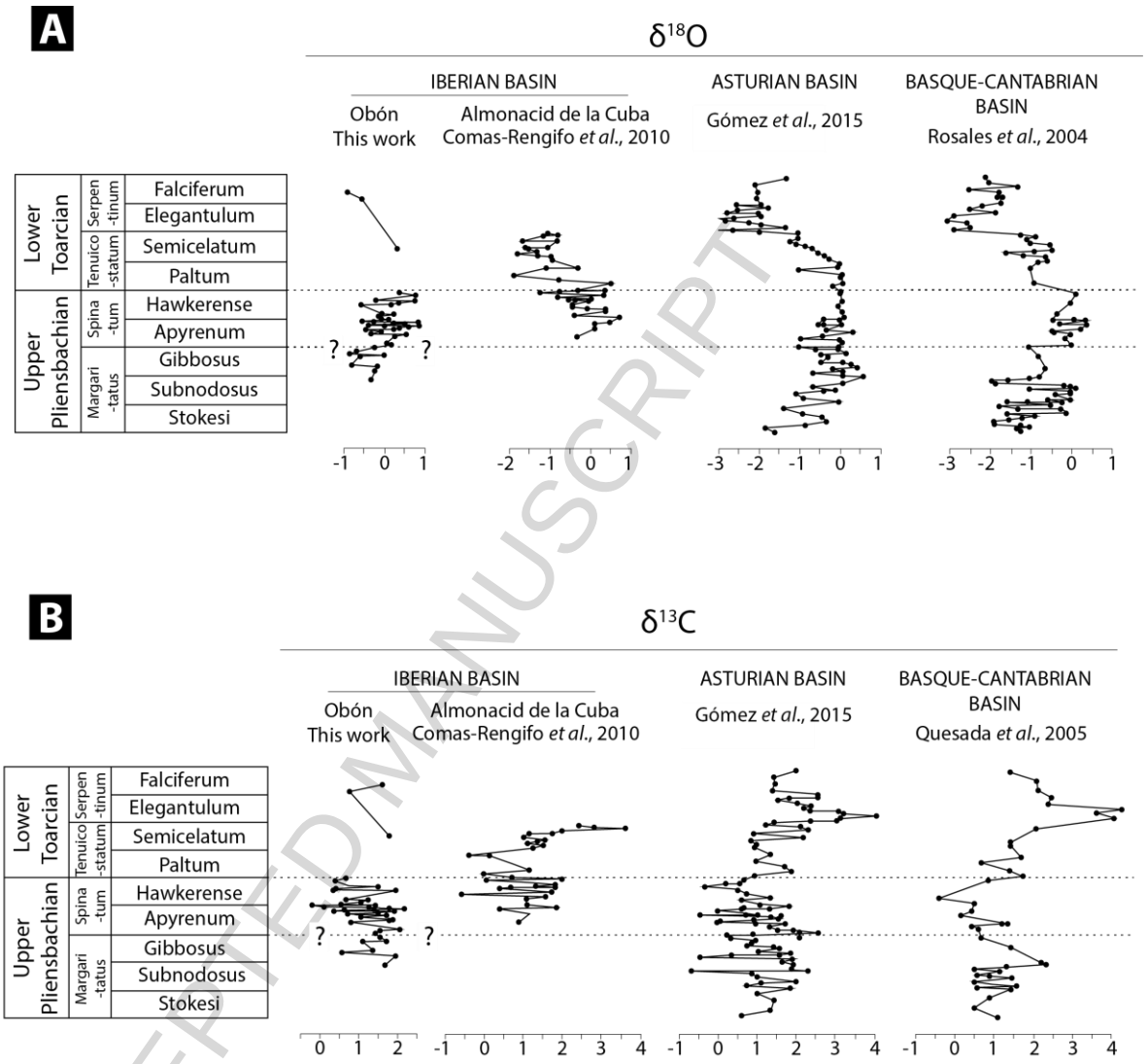

Figure 12

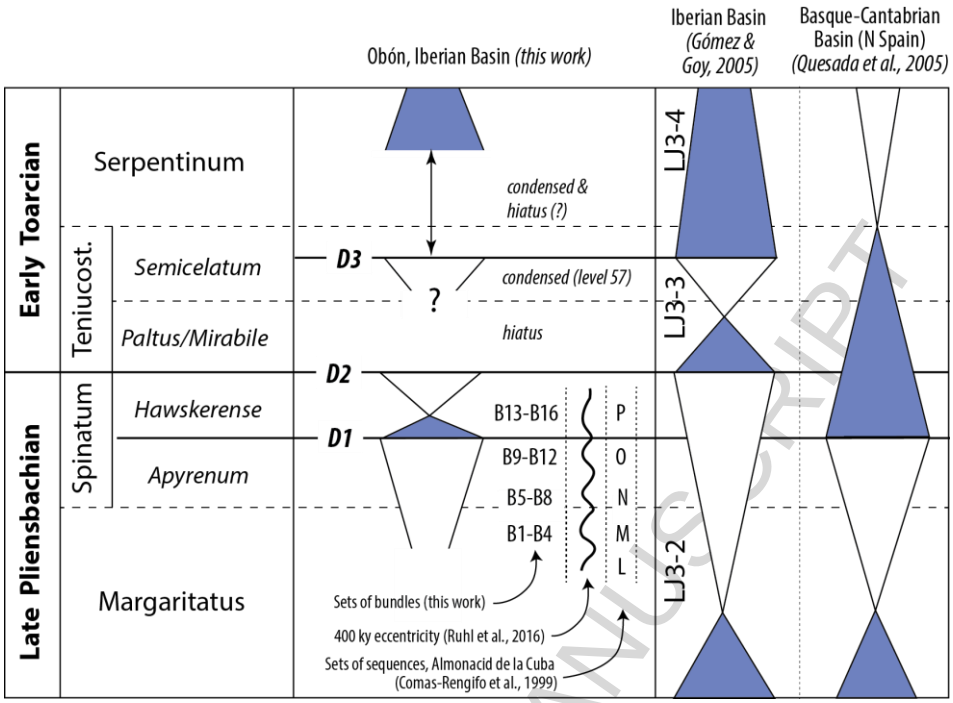

Figure 13

Table 1

Sample	Bed number	Type of sample	$\delta^{13}C$ (‰ V-PDB)	$\delta^{18}O$ (‰ V-PDB)	$^{87}Sr/^{86}Sr$	Ca (μg/g)	Fe (μg/g)	Mg (μg/g)	Mn (μg/g)	Na (μg/g)	Sr (μg/g)
OB-1-BL	1	Belemnite	1.69	-0.33	0.707151						
OB-1-BR	1	Brachiopod	0.99	-2.17							
OB-1-RT	1	Bulk rock	0.1	-2.87							
OB-2-BR	2	Brachiopod	1.24	-1.65							
OB-2-RT	2	Bulk rock	0.85	-2.19							
OB-3-BR	3	Brachiopod	1.65	-1.41							
OB-4a-BR	4	Brachiopod	1.37	-1.95							
OB-4a-RT	4	Bulk rock	0.56	-2.2							
OB-4b-BR	4	Brachiopod	1.55	-1.94	0.707251						
OB-5-BL	5	Belemnite	1.97	-0.22							
OB-6b-BL	6	Belemnite	1.14	-0.17		346652	0 (*)	2063	0.89 (*)	1509	1078
OB-7-BL	7	Belemnite	1.36	-0.81	0.707191						
OB-15-BR	15	Brachiopod	1.67	-2.02		350935	600	1076	3.53 (*)	653	544
OB-15b-BL	15	Belemnite	1.09	-0.61							
OB-15c-BL	15	Belemnite	1.75	-0.01							
OB-16-BL	16	Belemnite	1.41	-0.85							
OB-16a-BR	16	Brachiopod	1.37	-2.33							
OB-16b-BR	16	Brachiopod	2.17	-1.2	0.707177						
OB-17-BR	17	Brachiopod	1.75	-1.76							
OB-17-RT	17	Bulk rock	1.23	-1.74							
OB-18-BL	18	Belemnite	1.51	-0.67							
OB-25-BL	25	Belemnite	1.39	-0.24							
OB-25a-BR	25	Brachiopod	2.03	-1.51							
OB-25a-RT	25	Bulk rock	1.34	-2.09							
OB-26-BL	26	Belemnite	1.54	0.16	0.707157						
OB-26-BR	26	Brachiopod	1.77	-2.45							
OB-26-RT	26	Bulk rock	1.37	-2.21							
OB-27-BL	27	Belemnite	2.03	0.04							
OB-27-BR	27	Brachiopod	2.32	-1.16		345268	228 (*)	2535	7.87 (*)	748	557
OB-27a-BR	27	Brachiopod	2.08	-1.83							
OB-27a-RT	27	Bulk rock	1.32	-1.66							

Sample	Bed number	Type of sample	$\delta^{13}C$ (‰ V-PDB)	$\delta^{18}O$ (‰ V-PDB)	$^{87}Sr/^{86}Sr$	Ca (μg/g)	Fe (μg/g)	Mg (μg/g)	Mn (μg/g)	Na (μg/g)	Sr (μg/g)
OB-27b-BR	27	Brachiopod	2.4	-1.17							
OB-27b-RT	27	Bulk rock	1.21	-2.16							
OB-34-BL	34	Belemnite	0.76	0.23	0.707144						
OB-36-BR	36	Brachiopod	0.96	-2.17							
OB-36-RT	36	Bulk rock	0.63	-3.69							
OB-36a-BL	36	Belemnite	1.81	0.54							
OB-36b-BL	36	Belemnite	1.9	-0.33		337383	0 (*)	1739	0 (*)	1500	1071
OB-38-BL	38	Belemnite	1	-0.09							
OB-38-BR	38	Brachiopod	1.34	-1.34							
OB-39a-BL	39	Belemnite	1.77	-0.48							
OB-39a-BR	39	Brachiopod	1.44	-1.82							
OB-39a-RT	39	Bulk rock	1.08	-1.74							
OB-39b-BL	39	Belemnite	2.14	0.36							
OB-39b-BR	39	Brachiopod	0.67	-1.58	0.707137						
OB-39c-BL	39	Belemnite	1.04	0.13							
OB-39c-BR	39	Brachiopod	1.3	-1.4							
OB-39c-RT	39	Bulk rock	0.89	-1.27							
OB-39e-BL	39	Belemnite	1.35	0.04							
OB-40a-BL	40	Belemnite	1.46	0.34							
OB-40b-BL	40	Belemnite	1.59	0.61		342913	0 (*)	1696	1.09 (*)	1880	1084
OB-40c-BL	40	Belemnite	0.64	0.34							
OB-41a-BL	41	Belemnite	1.93	0.85							
OB-41b-BL	41	Belemnite	0.93	-0.01							
OB-41c-BL	41	Belemnite	0.69	-0.03							
OB-41d-BL	41	Belemnite	0.24	-0.43							
OB-42a-BL	42	Belemnite	0.6	-0.3		349388	0 (*)	2194	0 (*)	1561	1134
OB-42b-BL	42	Belemnite	1.38	0.49							
OB-43-	43	Brachiopod	1.88	-1.29		35993	1063	1969	18.8	578	509

BR						8			(*)		
OB-43a-BL	43	Belemnite	2.17	0.12	0.707105						
OB-43b-BL	43	Belemnite	1.92	0.55							
OB-43c-BL	43	Belemnite	1.77	0.17							
OB-43d-BL	43	Belemnite	1.54	0.31							
OB-43e-BL	43	Belemnite	1.54	0.83							
OB-44-BR	44	Brachiopod	1.03	-1.62							
OB-44a-BL	44	Belemnite	1.26	-0.18	0.707105						
OB-44b-BL	44	Belemnite	1.1	-0.48							
OB-45-BL	45	Belemnite	-0.25	0.19							
OB-46a-BL	46	Belemnite	1.46	0.12	0.707107						
OB-46b-BL	46	Belemnite	0.49	0.01							
OB-48-BR	48	Brach. (**)	1.11	-1.81	0.707196	378180	2117	3068	42.3	338	273
OB-48-RT	48	Bulk rock	0.41	-2.99							
OB-48a-BL	48	Belemnite	1.14	-0.07		343115	0 (*)	2208	0 (*)	1787	1266
OB-49a-BL	49	Belemnite	1.23	0.32							
OB-49c-BL	49	Belemnite	0.69	0.03	0.707091						
OB-53a-BL	53	Belemnite	0.26	0.31							
OB-53b-BL	53	Belemnite	1.97	-0.49	0.707066						
OB-53c-BL	53	Belemnite	0.37	0.42							
OB-54-55a	54	Belemnite	1.44	0.81							
OB-54-55b	54-55	Belemnite	0.74	-0.14	0.707083	342287	0 (*)	1924	0 (*)	1199	923
OB-56a-BL	56	Belemnite	0.36	0.8	0.707070						
OB-56b-BL	56	Belemnite	0.74	0.41							
OB-57-BL	57	Belemnite	1.77	0.36	0.707066						
OB-57-BR	57	Brachiopod	0.28	-1.72							
OB-57-RT	57	Bulk rock	-0.38	-1.95							
OB-59-BR	59	Brachiopod	1.29	-2.02	0.707215	368688	428	2479	25.1	1549	760
OB-59-RT	59	Bulk rock	-0.23	-2.86							
OB-60-BR	60	Brachiopod	1.86	-1.48	0.707230	340041	337	2413	13.4 (*)	419	414

OB-60-RT	60	Bulk rock	0.19	-1.97	
OB-62-BL	62	Belemnite	0.76	-0.47	
OB-63-BR	63	Brachiopod	1.52	-2.2	0.707235
OB-65-BL	65	Belemnite	1.62	-0.82	0.707209

(*) Values below detection limits (**) Sample considered to be altered on the basis of geochemical results